Terahertz Imaging and Sensing Applications With Silicon-Based Technologies

Philipp Hillger, *Student Member, IEEE*, Janusz Grzyb, Ritesh Jain,
and Ullrich R. Pfeiffer, *Senior Member, IEEE*

(Invited Paper)

***Abstract*—Traditional terahertz (THz) equipment faces major obstacles in providing the system cost and compactness necessary for widespread deployment of THz applications. Because of this, the field of THz integrated circuit (THz IC) design in CMOS and SiGe HBT technologies has surged in the last decade. An interplay of advances in silicon process technology, design technique, and microelectronic packaging promises to narrow the gap between the requirements and the reality of system cost and performance of THz components. Furthermore, the scalability, reconfigurability, and signal processing features of silicon technology have initiated research in complex THz ICs that expand the functionality of THz systems; this has enabled new applications, methods, and algorithms. This paper reviews the progress in THz IC research and investigates several realizations of THz imaging and sensing applications with silicon-based components regarding their motivation, system performance, and challenges. THz computed tomography, broadband multicolor imaging, high-resolution FMCW radar imaging, subwavelength resolution near-field imaging, and compressed sensing are presented.**

***Index Terms*—CMOS, computed tomography (CT), compressed sensing, FMCW radar, multicolor imaging, near-field imaging, silicon technology, SiGe BiCMOS, terahertz (THz), THz imaging.**

I. INTRODUCTION

THE most pervasive applications for terahertz (THz) waves are in the areas of radio astronomy and earth observation. Here, high-sensitivity heterodyne receivers are used to investigate the molecular composition and dynamics of the interstellar medium and earth's atmosphere [1]. The instrumentation for these applications is based on either traditional LO-driven Schottky-diode mixers, which can reach sensitivities around 50 times the quantum limit at room-temperature below 3 THz [2]–[4], or on sophisticated detector technology that requires cryogenic cooling. Such detectors, including superconductor-insulator-superconductor devices, hot electron bolometers, and Josephson junctions, show tremendous sensitivity close to the quantum limit [3], [5]. Yet, the implications of the cooling requirements on system weight, turn-ON time, and cost have impeded the transfer of this technology to a majority of commercially deployable THz systems.

Markets and applications are projected to be fairly diverse for the terrestrial use of THz waves [6]. The uses span from potential large-volume applications, such as high-speed wireless communications [7] and radar gesture control [8] to small-volume niches in security inspection [9] and medical diagnosis [10]. This requires a diverse range of technology solutions, as an all-in-one technology platform that offers high performance, low cost, and compactness at the same time does not exist yet.

Today's available THz equipment can be divided into pure electronic and optoelectronic-based solutions. The electronic solutions rely primarily on split-block hallow waveguide assemblies with Schottky diodes and III–V devices or on micromachined bolometer arrays. There are various remarkable advances in this field, including the commercial development of GaAs Schottky-diode-based multiplier sources, delivering up to 35 μW at 1.9 THz [11], and the first demonstration of amplification above 1 THz using an InP-HEMT technology, with an $f_{\max}$ around 1.5 THz [12]. Still, because of noncompatibility with conventional microelectronic packaging, or the necessity of adequate cooling, such THz electronics mostly target performance-driven niches. For example, passive imaging systems based on InP HEMT low-noise preamplification [13], [14] or kinetic inductance bolometer arrays [15], and active radar imaging systems based on Schottky diodes [16], show great potential for imaging applications that can tolerate costly and stationary systems, such as mass transit security and loss prevention. Moreover, electronic THz systems for real-time active transmission imaging are already commercially available for applications, such as conveyor belt imaging [17] or the security screening of letters and packages [18].

In the field of optoelectronic THz equipment, THz time-domain spectroscopy systems have emerged as a valuable laboratory tool for fundamental THz science and imaging [19], [20]. They offer the extraction of dispersive transmission and reflection properties of different materials in more than a decade of bandwidth. Furthermore, continuous-wave (CW) sources based

---

Manuscript received September 23, 2018; revised November 8, 2018 and November 30, 2018; accepted November 30, 2018. Date of publication December 14, 2018; date of current version January 9, 2019. This work was supported in part by the German Research Foundation within the frame of the Reinhart Koselleck Project, in part by the program ESSENCE under Grant SPP 1857, in part by the program CoSIP under Grant SPP 1798, and in part by the SFB/Transregio 196 MARIE Project C04/C08. *(Corresponding author: Ullrich R. Pfeiffer.)*

The authors are with the Institute for High-Frequency and Communication Technology, University of Wuppertal, Wuppertal D-42119, Germany (e-mail: hillger@uni-wuppertal.de; grzyb@uni-wuppertal.de; rjain@uni-wuppertal.de; ullrich@ieee.org).

Color versions of one or more of the figures in this paper are available online at http://ieeexplore.ieee.org.

Digital Object Identifier 10.1109/TTHZ.2018.2884852

on quantum cascade lasers can now generate up to 1 W of power at 3.4 THz. These sources, however, similarly require cooling and their operation is limited to frequencies above 2 THz [21].

In summary, it can be stated that the aforementioned THz platforms all suffer from distinct drawbacks for mass deployment, including system cost, achievable integration level or reliability. Most importantly, the currently utilized microelectronic packaging techniques for electronic THz systems cannot easily support the tight tolerance levels required for THz applications and are not scalable to large volumes. Low-cost THz applications, therefore, require single-chip solutions that obviate the need for complex microelectronic assembly. THz integrated circuits (THz ICs) based on modern nanoscale CMOS and SiGe HBT/BiCMOS process technologies promise to fulfill this role, at least in the lower end of the THz spectrum. They concurrently offer economies of scale, small form-factors, and unprecedented integration capability at the highest industry standards. THz ICs are, therefore, an interesting option for applications that require extremely compact THz microsystems for sensing [22]–[24] or active imaging components at a reasonable price-performance ratio [25], [26]. In this regard, it is also important to note the ongoing research activities on the heterogeneous integration of III–V devices with foundry-level silicon technology [27], which show enormous potential for future medium-sized THz markets.

However, the benefits of economic viability and system size are not the only drivers for research in THz ICs. The design space that opens up by device plurality, reconfigurability, and THz-mixed signal cointegration promises to expand the functional scope of THz imaging systems. Applications such as THz-light field imaging based on CMOS detector focal-plane arrays (FPAs) [28], real-time subwavelength imaging with integrated near-field arrays [29], and broadband passive spectroscopy [30], have all been demonstrated based on THz ICs that approach integration-levels comparable to the ones exhibited in conventional consumer electronics.

At present, the low speed of silicon transistors and the issues related to efficient THz signal escape [31] constitute an ongoing research challenge for both technology development and IC design. Over time, silicon technology has undergone a steady scaling and an improvement of device parasitics, recently achieving an $f_{\max}$ of 500 GHz in commercially available 0.13-μm SiGe BiCMOS technology [32]. While these advances have already kicked off the large-scale commercialization of various mmWave systems, such as 60-GHz transceivers for the wireless backhaul [33] and 77-GHz automotive radar [34], past research has shown that THz IC design cannot only be a mere extension of classic radio-frequency design techniques to THz frequencies, but it rather requires novel circuit architectures to circumvent the device-speed limitations. For example, the most significant progress toward practical source power levels has been achieved by the large-scale implementation of THz subcircuits that exploit a codesign approach of electromagnetic structures and active circuitry for power combining and wavefront engineering [35]–[39].

In this paper, we aim to assess the current capabilities and performance of THz ICs for imaging and sensing applications. First, the state of the art in source and detector/receiver THz ICs is examined in Section II. Section III discusses practical realizations of several imaging and sensing systems in silicon technology. Final conclusions and outlook are presented in Section IV.

II. STATE-OF-THE-ART SILICON THz ICs

This section first briefly discusses recent progress in high-speed silicon technology. Next, the state of the art and performance trends of silicon-based THz source and receiver components are reviewed.

A. Silicon Process Technologies for THz ICs

Fueled by the investments in the multibillion dollar consumer markets for digital microprocessors and radio-frequency integrated circuits (RFICs), CMOS technology undergoes continuous gate-width scaling, which simultaneously increases the intrinsic speed of MOSFETs as a by-product. However, the maximum frequency of oscillation ($f_{\max}$) of fully wired n-MOSFETs decreases for the most advanced CMOS nodes ($<$ 45 nm) because of a scaling-related deterioration of gate and wiring resistances [40]. This has damped the expectations that future deep nanoscale CMOS technology can provide to reliable fundamental device operation in the THz band [6]. Meanwhile, the low power handling capabilities of MOSFETs reinvigorated SiGe HBT technology as a bridging technology offering a low-cost alternative to III–V MMICs in the mm-wave band. With commercially available high-speed SiGe HBT technology achieving 500 GHz $f_{\max}$ [32], and with research activities demonstrating 700-GHz $f_{\max}$ for the next technology node [41], SiGe HBT technology is just on the verge of enabling fundamentally operated circuits above 300 GHz [42]–[44]. Contrary to CMOS technology, the speed of SiGe HBT devices is projected to continue to improve with transistor scaling. Results obtained from a theoretical analysis of the electrical performance limits of SiGe HBTs indicate that operating frequencies of 1 THz and beyond are within reach in the future [6].

However, the scaling of silicon technology poses considerable challenges for THz IC integration. First, advances in frequency performance are inherently linked to a reduction in device breakdown voltages. For high-speed 130-nm SiGe-HBT technology, the open-base collector-emitter breakdown voltage is $BV_{\text{ceo}} = 1.6$ V [32], whereas CMOS technology exhibits gate-oxide breakdown voltages of only 1.2 V for the 65-nm node [45] and below for more advanced nodes. Second, the technology stack of foundry-level silicon technology presents an increasingly unfavorable environment for antenna and passives implementation in the THz band. Typically, several metal layers are embedded in a thin dielectric stack (BEOL) on top of a lossy silicon substrate. The BEOL fabrication enforces strict design rules on the density of metal structures, which escalate the modeling and design effort of on-chip antennas and passives. The design of on-chip antennas in silicon technology is particularly challenging given potential multimode propagation issues (e.g., surface waves) [46], [47] and the difficulties in achieving appropriately high directivity of the antenna system

TABLE I
State of the Art of Silicon-Integrated Radiation Sources Above 250 GHz

Unlocked oscillator based sources

Technology	Frequency [GHz]	Circuit Architecture	Antenna	Tot. rad. power [dBm]	P_{dc} [mW]	Ref.
65 nm CMOS	247–272	4 locked osc. + 8 2-push osc.	8 slots + si. lens	0.5	800	[54]
45 nm CMOS	276–285	osc. + x2 + H2 extraction	16 distributed active radiators	-7.2	820	[35]
65 nm CMOS	283–288	2 locked 3-push ring osc.	ring + si. lens	-4.1	275	[55]
65 nm CMOS	284–301	osc. + H3 extraction	ring	-2.7	19.2	[56]
130 nm SiGe HBT	305–375	2-push osc. + PA + x2	patch	0	1700	[57]
65 nm CMOS	312–315	half-quadrature osc. + 4 IL-x4	4 slots + ceramic	0.8	298	[58]
130 nm SiGe HBT	332–352	4 standing-wave 4-push osc.	4 patches	-10.5	425	[38]
65 nm CMOS	337–339	16 locked 4-push osc.	16 patches	-0.9	1540	[36]
130 nm SiGe HBT	426–437	Colpitts osc. + x2	circular-slot + si. lens	-6.3	165	[52]
130 nm SiGe HBT	490	3-push Colpitts osc.	circular slot + si. lens	-14.2	45	[59]
130 nm SiGe HBT	519–536	2 locked 3-push Colpitts osc.	ring + si. lens	-12	156	[53]
28 nm CMOS	524–555	cross-coupled osc. + x3	ring + dielectric lens	-22	19	[60]
65 nm CMOS	609–624	osc. + H5 extraction	ring	-23	17	[61]
130 nm SiGe HBT	1010–1016	42 coupled osc. + H4 extraction	42 slots + si. lens	-10.9	1100	[39]

Locked oscillator and multiplier chain based sources

Technology	Frequency [GHz]	Circuit Architecture	Antenna	Tot. rad. power [dBm]	P_{dc} [mW]	Ref.
130 nm SiGe HBT	210–270	fund. amp.	dual-polarized slot + si. lens	5	-	[42]
130 nm SiGe HBT	220–260	fund. IQ mix. + PA	ring + si. lens	8.5	960	[7]
130 nm SiGe HBT	317	16 locked 2-push driven by 160 GHz PLL	16 slots	5.2	630	[37]
45 nm bulk CMOS	370–410	8-element Array of PA + x4	8 patches	-7	1500	[62]
45 nm bulk CMOS	395–435	8-element x4	8 slots + quartz	-10	700	[63]
65 nm bulk CMOS	540–550	locked 3-push colpitts osc.	circular slot + si. lens	-27	174	[64]
65 nm bulk CMOS	582–612	x2 + PA + x3 + PA + x5	ring	-15.1	378	[65]
65 nm CMOS	650-730	x5 SVAR	patch	-21.3	-	[66]
250 nm SiGe HBT	820–845	4 path, x3 + PA + x3 + PA + x5	4 diff. patches	-29	3700	[67]
130 nm SiGe HBT	920-944	x4	2 patches	-17.3	5.7	[51]
65 nm CMOS	1300-1460	x5 SVAR + x2 ASVAR	2 patches	-22.7	-	[68]

to provide sufficient link budget for practical applications. This motivated the wide use of backside radiating on-chip antennas with auxiliary silicon lenses [31], [48].

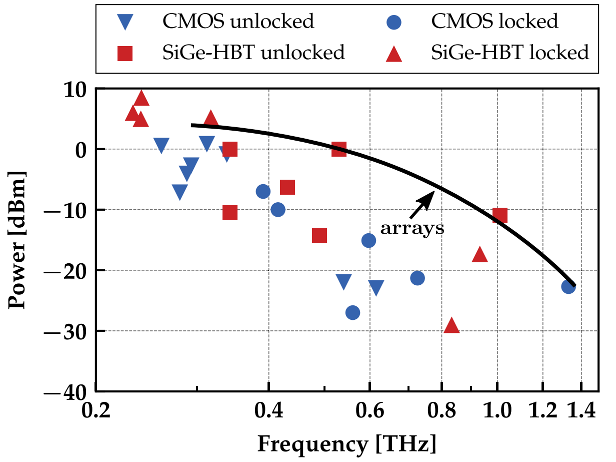

Fig. 1. Comparison of state-of-the-art THz sources in CMOS and SiGe technologies.

B. Sources

Since the first demonstration of a CMOS THz source ten years ago [49], which radiated -42 dBm at 410 GHz, tremendous progress has been made toward the provision of suitable power levels for imaging applications with THz ICs. The advances were enabled by both new design methodologies for the proper synthesis of passive embedding networks to optimize the harmonic generation [50]–[52] and novel scalable system architectures [36], [37], [39], [53]. Table I and Fig. 1 summarize the current state of the art for CMOS and SiGe HBT radiation sources above 250 GHz. The sources are grouped into unlocked oscillator-based sources [35], [36], [38], [39], [52]–[61] and into oscillator- or multiplier-chain-based sources that can be locked to an external phase-stable reference signal [7], [37], [42], [51], [62]–[68]. The table furthermore lists the applied circuit architectures and antennas to emphasize a remarkable variety between different implementations. It is worth noting that no single best architecture has emerged yet and researchers continue to explore a large design space offered by silicon technologies to overcome the barriers associated with the limited device speed and with THz wave escape from the chip level [31].

Currently, the upper frequency limit for fundamental circuit operation for the fastest 130-nm SiGe HBT technology with $f_{\max} = 500$ GHz [32] is just below the mmWave-THz transition. Total radiated power (TRP) levels up to 8.5 dBm have been demonstrated for power-amplifier-based transmitter front-ends at 240 GHz, with a 3-dB bandwidth of 35 GHz in an experimental 130-nm SiGe-HBT technology with $f_T/f_{\max} =$ 350 GHz/550 GHz [7]. Above 300 GHz, silicon THz sources employ the nonlinear frequency translation process of strongly driven high-speed devices. The nonlinear THz front-end circuit is either directly implemented as a harmonic N-push oscillator or as a frequency multiplier circuit. Both approaches entail a conversion loss that increases rapidly with the harmonic order and drive frequency. Therefore, contrary to the typical 20 dB/decade

TABLE II
STATE OF THE ART OF SILICON-INTEGRATED SUB-mmWAVE AND THz RECEIVERS

Direct detectors

Detector type	Frequency [GHz]	Antenna	Max. Responsivity	Min. NEP[1] [pW/$\sqrt{Hz}$]	Ref.
130 nm SiGe HBT	260	diff. ring	2600 kV/W	8.4	[47]
Shottky diode in 130 nm CMOS	280	patch	5.1 kV/W	29	[87]
130 nm SiGe HBT	315	dipole	6.1 kV/W	21.2	[83]
180 nm SiGe HBT	320	diff. slot + quartz superstrate	18 kV/W	34	[84]
90 nm NMOS	365	h-shaped dipole	185 kV/W	40	[75]
150 nm NMOS	595	patch	0.35 kV/W	42	[76]
130 nm NMOS	600	bow-tie	216 kV/W	25.9	[77]
Shottky diode in 130 nm bulk CMOS	860	patch	0.273 kV/W	42	[87]
65 nm SOI NMOS	650	folded dipole + si. lens	1.93 kV/W	17	[78]
130 nm NMOS	650	diff. ring + si. lens	0.45 kV/W	80	[79]
250 nm SiGe HBT	700	diff. ring + si. lens	1 A/W	50	[85]
65 nm NMOS	724	diff. ring + si. lens	2.2 kV/W	14	[80]
Contact in 45 nm CMOS	781	patch	0.558 kV/W	56	[93]
Diode-NMOS in 130 nm CMOS	823	patch	2.56 kV/W	36.2	[94]
65 nm bulk NMOS	856	diff. ring + si. lens	140 kV/W	100	[81]
180 nm NMOS	860	patch	3.3 kV/W	106	[82]

Heterodyne and homodyne receivers

Technology	Frequency [GHz]	Circuit Architecture	Antenna	Conversion Gain [dB]	Single-Sideband Noise Figure [dB]	Ref.
130 nm SiGe HBT	240	fund. mixer-first	double folded-dipole	7–32	13.4	[44]
65 nm CMOS	240	fund. IQ mixer-first	loop	25	15	[88]
130 nm SiGe HBT	240	fund. IQ mixer-first	ring + si. lens	8	12-14	[89]
65 nm CMOS	260	fund. IQ mixer-first	leaky wave	17	19	[90]
40 nm CMOS	335	fund. IQ mixer-first	patch	-1.7	23.2	[91]
130 nm SiGe HBT	650	4^{th}-harmonic mixer	folded-dipole	-13	42	[92]
250 nm SiGe HBT	820	5^{th}-harmonic mixer	diff. patch	-22	47	[67]
250 nm SiGe HBT	650 820 995	2x2 array of harmonic mixers, simultaneous operation in 6 bands	ring + si. lens	-21 -18 -23	44 45 47	[26]

[1] The table lists the optical NEP and antenna gain is de-embedded.

roll-off for power amplifiers below $f_{\max}$ (Johnson Limit) [69], the data-points indicate an around 40 dB/decade power roll-off for single-radiator sources in the THz band.

Notably, the small size of on-chip THz passives and the abundant availability of transistors have motivated the research in coherent single-chip multielement radiators. Innovative device/electromagnetics codesign architectures that utilize synchronized two-dimensional (2-D) oscillator arrays broke the power roll-off trend, delivering a TRP of up to 5.2 dBm at 317 GHz with a 16-element array [37] and -10.9 dBm at 1.01 THz with a 42-element array [39] in 130-nm SiGe HBT technology. Furthermore, the baseband processing capabilities of silicon technology have been further exploited for radiation pattern reconfiguration of multielement sources with the aid of power-on control of asynchronous sources to diffuse scene illumination at 530 GHz [53] or phased array functionality at 338 GHz [36] and 400 GHz [62].

C. Receivers

Similarly to the first silicon-based THz source demonstrations, the first silicon-based THz FPA was demonstrated ten years ago [70]. Since then, the research in silicon THz IC receivers is largely focused on advancing the sensitivity and bandwidth of direct power detectors. Silicon technology features high fabrication yield and the availability of on-chip baseband processing circuits, enabling the integration of detectors into chip-scale FPA with on-chip read-out circuitry. Therefore, silicon detectors offer significantly higher integration capabilities compared with the prevalent room-temperature THz detector technologies, such as Schottky barrier diodes, InP HEMT low-noise amplifiers, Golay-cells, microbolometers, and pyroelectric detectors [71]–[74].

Due to the lack of low-noise preamplification in the THz band, silicon power detectors are implemented as antenna-coupled direct detectors. Therefore, the predominantly exploited methods for THz direct detection are either non-quasistatic self-mixing in cold MOSFET channels [75]–[82] or rectification in the base-emitter junction of a high-speed HBT [47], [83]–[85]. At THz frequencies, both device classes operate close-to or above their cutoff frequencies defined by the carrier transit time, and their response and operation bandwidth are severely influenced by the efficiency of coupling the THz radiation into the intrinsic device. Since broadband operation is typically desired for practical implementations to allow versatile application scenarios at low cost, classic narrowband RF matching techniques made way for innovative antenna-device codesign approaches. In particular, antenna systems based on a backside-radiating on-chip primary antennas and an external hyper-hemispherical silicon lenses have been demonstrated to simultaneously provide pW/$\sqrt{\text{Hz}}$-level noise-equivalent power (NEP) across several hundreds of GHz and antenna directivity values in the range of 20 dBi [78]–[81], [85].

MOSFET direct power detectors are operated without drain-source bias (“cold”) and in moderate inversion for the highest responsivity. The lowest reported NEP is in the range of 12–14 pW/$\sqrt{\text{Hz}}$ with a 3-dB RF operation band of around 650–1000 GHz in 65-nm CMOS [80]. Please note that although device scaling can result in lower thermal noise of the MOSFET channel, the so far reported detector performance (responsivity, NEP, operation bandwidth) did not considerably improve by migration to nanometric CMOS technology nodes. One of the main possible reasons for that is the very high (kΩ-range) and frequency-dependent impedance of the MOSFET operating in moderate inversion, which makes efficient and broadband coupling to on-chip antenna very challenging. Contrary to that, the impedance levels associated with a base-emitter junction of HBTs at THz frequencies should facilitate considerably broader frequency operation range, although the literature still reports very few implementations of such detectors at THz frequencies. An NEP of 15 pW/$\sqrt{\text{Hz}}$ and 50 pW/$\sqrt{\text{Hz}}$ was reported at 540 and 700 GHz, respectively, for 130- and 250-nm SiGe HBT technology nodes [85], [86] and further base-emitter junction optimization should result in substantial improvements of detector performance. Schottky diodes in CMOS technology were also reported for THz signal rectification at 860 GHz with an NEP of 42 pW/$\sqrt{\text{Hz}}$ [87]. However, power detectors in silicon technologies still lack the sensitivity requirements regarding noise-equivalent temperature difference (NETD) for passive imaging (NETD < 0.5 K) and are in need for artificial illumination. To reach the required NETD, an estimated detector NEP in the range of 1 pW/$\sqrt{Hz}$ combined with a large fractional bandwidth of multiple hundreds of GHz is necessary, which constitutes an ambitious objective for future work.

Hetero-/homodyne receivers in silicon technologies above 300 GHz are still very scarce. They rely on a mixer-first architecture with predominantly subharmonic operation and low instantaneous IF bandwidth, yielding relatively poor conversion gain and noise figure. Thereby, implementation issues such as the LO distribution and the total dc power consumption have thus far been prohibitive for large-scale array implementation. Table II lists some of related works to indicate the typical performance metrics [26], [44], [67], [88]–[92] and Fig. 2 shows the sensitivity comparison between state-of-the-art direct detectors and coherent hetero-/homodyne receivers.[1]

The hetero-/homodyne receivers show distinctly better sensitivity by around 80 dB at 300 GHz, as compared to direct detectors. The necessity of using higher harmonic orders to reach higher operation frequencies, however, results in a steep noise figure increase. It is important to note that a similar trend is not present for direct power detectors.

III. THz IMAGING APPLICATIONS

This section presents some case studies on silicon-based components for THz imaging and sensing applications. This paper is by no means comprehensive, but it should provide the reader with a grasp of current system performance and future directions.

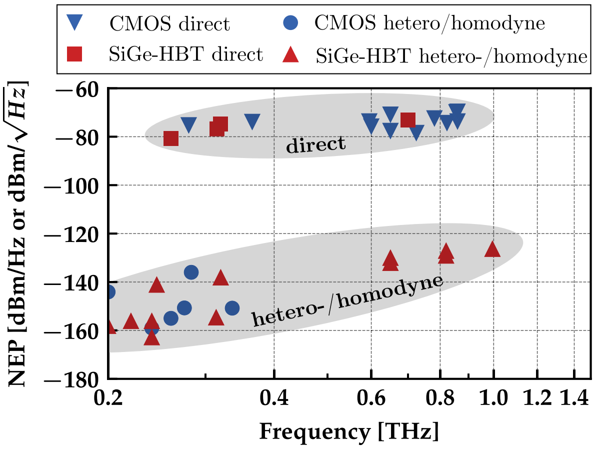

Fig. 2. Comparison of state-of-the-art direct power detectors and heterodyne/homodyne receivers in CMOS and SiGe technologies in the frequency range of 0.2 THz to 1 THz. The comparison basis relies on NEP in units of dBm/Hz$^{0.5}$ for direct power detectors and NEP in units of dBm/Hz for hetero-/homodyne receivers.

A. *Computed Tomography (CT)*

Since the first demonstration of THz transmission imaging by Hu and Nuss in 1995 [95], most studies on THz imaging were focused on 2-D imaging. Because 2-D imaging only provides limited information content for thick objects with high volumetric complexity, there has been an increasing effort to extend THz imaging modalities to 3-D imaging. 3-D visualization of the objects' internal structure may be particularly valuable for applications in industrial quality control, e.g., for the localization of cracks and defects in composite materials, or for content inspection of the packaged goods. Another interesting use case for 3-D THz imaging could arise for noninvasive analysis of archaeological findings, e.g., inspection of wrapped mummies [96], sealed pottery [97], or imaging of human bones [98].

Various techniques have been investigated for the acquisition of 3-D images at THz frequencies, including time-of-flight measurements in reflection mode [99], diffraction tomography [100], tomosynthesis [99], imaging with binary lenses [101], and CT with ultrashort THz pulses [102] or CW sources [97].

THz tomography competes against the highly established X-ray CT, which usually provides far superior image quality in terms of spatial resolution and uniqueness to the image contrast mechanism. However, there are two opportunities for THz frequencies in this field. First, THz waves may provide valuable supplemental information, enabling additional extraction of the spectroscopic object properties [102] and providing different absorptive contrast as compared to X-rays. Next, ongoing advances in silicon-integrated THz components, outlined in Section II, should enable the realization of ultra-low-cost 3-D THz-CT imaging systems [25], promising an increased exploitation for future industrial applications as compared to expensive

---

[1] The sensitivity figure of hetero-/homodyne detectors is typically reported in terms of noise-figure (NF), which is converted to an equivalent NEP after assuming room-temperature thermal noise as the receiver input, i.e., NEP $= -174$ dBm/Hz + NF (in dB), normalized to a 1-Hz bandwidth. Since the output IF signal is read out in terms of signal power, the resulting NEP is reported in the units of dBm/Hz. For direct detectors, the NEP is reported in the unit of dBm/$\sqrt{\text{Hz}}$ owing to the rectification of THz power to a dc voltage or current.

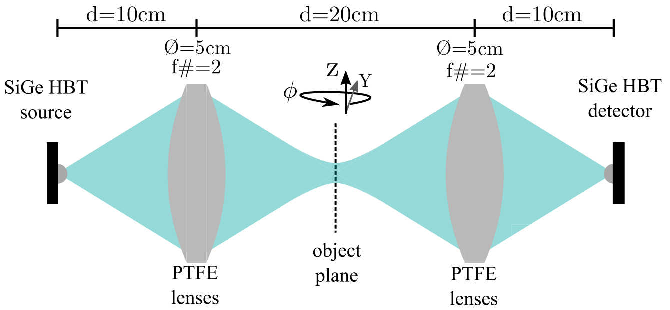

Fig. 3. Illustration of the simple low-cost THz-CT experiment. The setup comprises a 430-GHz SiGe HBT source, a SiGe HBT detector and an optical train of 4 $f_{\#} = 2$, 50-mm PTFE lenses. The object is rotated (ϕ) and stepped in the 2-D object plane (y, z).

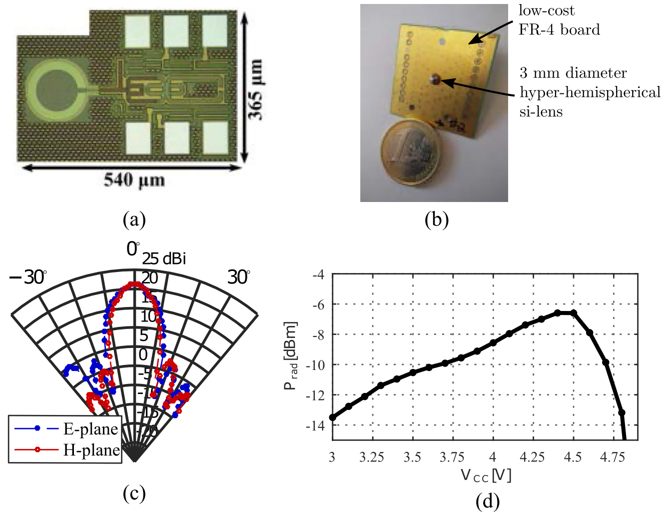

Fig. 4. 430-GHz source based on 130-nm SiGe HBT technology. (a) Chip micrograph; after [52]. (b) Image of a low-cost packaging scheme with secondary Si-lens antenna. (c) Measured radiation pattern; data from [52]. (d) Measured source output power; data from [52].

X-ray CT equipment with necessary security measures related to the hazardous radiation.

This paper demonstrates a THz-CT setup solely based on silicon components and simple THz optics. Fig. 3 illustrates $2f$–$2f$ transmission imaging setup for the volume data acquisition. A free-running radiation source based on a Colpitts-oscillator-driven antenna-coupled doubler with optimized harmonic feedback illuminates the object. The source radiates -6.3 dBm at 430 GHz and is implemented in 130-nm SiGe HBT technology [52]. The silicon die is equipped with an on-chip antenna illuminating the silicon lens through the chip backside to result in a directivity of ≈ 21 dBi, which is appropriate for coupling to an optical train based on 5-cm diameter PTFE lenses with 10-cm focal length. Fig. 4 summarizes some implementation and characterization details of the source. An in-house developed SiGe HBT power detector with the measured NEP of 9.5 pW/$\sqrt{\text{Hz}}$ and current responsivity of 1.25 A/W at 430 GHz, manufactured in an experimental 0.13-μm SiGe HBT technology with peak $f_t/f_{\max}$ of 350 GHz/550 GHz, is used to acquire the raster scanned 2-D transmission images of an object under different projection angles. The Gaussian $1/e^2$ beam waist in the object plane was measured with the knife-edge technique [103] and is 3 mm in y-direction and 3.2 mm in z-direction. A high dynamic range of 71.2 dB can be achieved by electronic chopping of the source at 120 kHz and 3-ms integration time of an external lock-in amplifier. A short performance summary of the THz-CT setup is given in Table III.

TABLE III
THz-CT PERFORMANCE SUMMARY

Operation frequency	426–437 GHz
Peak total radiated power	–6.3 dBm
Detector NEP	9.5 pW/$\sqrt{Hz}$
System dynamic range	71.2 dB
Lateral resolution	$\approx$ 3 mm

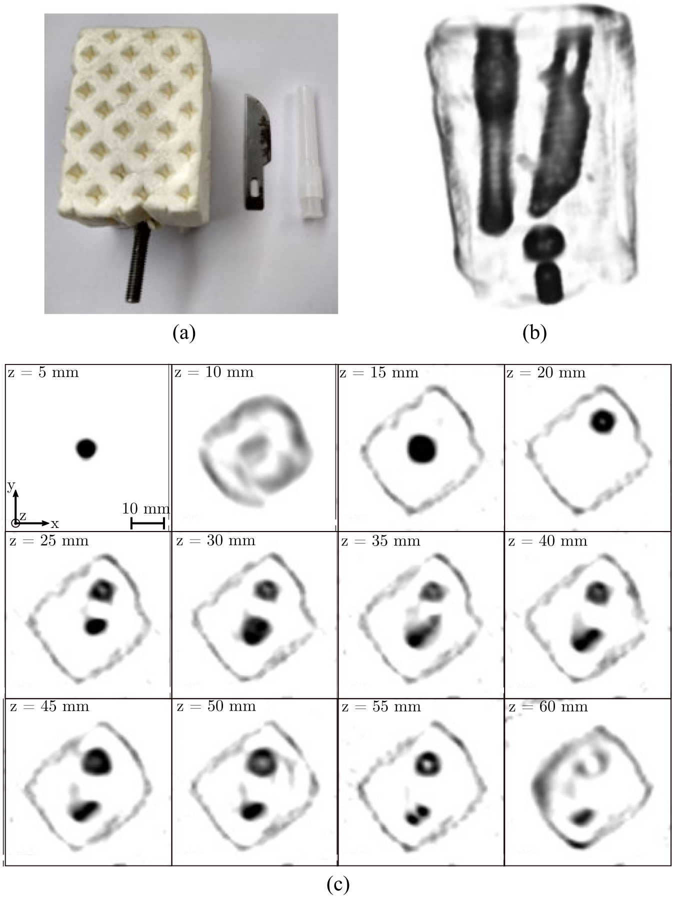

Fig. 5. CT-Imaging results for a knife blade and hypodermic needle embedded in polystyrene foam. (a) Visible-light photo. (b) 2-D volume render after tomographic reconstruction with SART algorithm [104]. (c) 2-D slices in x–y-plane for different heights (z-axis). The data was acquired with 1-mm spatial and 10° angular steps. The acquisition time was 282 min.

For demonstration purposes, a cuboid made of polystyrene with a metal knife blade and a hypodermic needle inside its protective casing was scanned. Fig. 5(a) shows a visible light photograph of the objects and Fig. 5(b) shows corresponding results of the volume render after tomographic reconstruction. A total of 18 projections were acquired in 282 min with a 10° angle resolution and a 1-mm step size. The projection size was 54 mm $\times$ 68 mm, leading to a total scanning speed of 11.7 mm^3/ s when referred to the volume after tomographic reconstruction. A reconstruction algorithm based on Simultaneous Algebraic Reconstruction Technique (SART) (360 iterations) from the *ASTRA Tomography Toolbox* [104] was applied to synthesize the 2-D slices shown in Fig. 5(c) at all heights. The algorithms currently do not account for quasi-optical effects at THz frequencies.

The simple low-cost THz-CT setup, although currently very slow, is capable of visualizing the macroscopic structure of the embedded objects with sufficient detail for object identification. However, a consequence of quasi-optical operation at THz frequencies is that the image contrast is not solely defined by on the absorption of the material but also by refraction and scattering at the object interfaces. This leads to an information ambiguity between absorption and refraction. As shown in Fig. 5(c), the polystyrene cuboid is reconstructed as a nonuniform material and the plastic casing of the needle exhibits a similar image contrast compared to the fully reflecting metal blade.

The long image acquisition time currently constitutes the main issue to adopt THz-CT as a tool for industrial quality control, where scanning times of several minutes are still unacceptable. Yet, rapid THz-CT volume acquisition within seconds has been readily demonstrated by 1-D and 2-D collimated beam object illumination with nonsilicon high-power sources and concurrent FPA detection [105], [106].

B. Imaging With Compressed Sensing

Compressed sensing (CS) is a signal processing concept that deals with the reconstruction of sparse information from undersampled signals. In contrast to the postprocessing compression methods (e.g., JPEG in images, MP3 in Audio), CS deals with measuring the compressed signal directly, thereby saving on the measurement time. CS can be utilized to build a single-pixel camera (SPC), where the light incident on a scene or an object is modulated spatially and thereafter integrated over a single-pixel sensor [107]. Therefore, a 2-D pixel array is not required at the sensing plane, saving on the size and complexity, which allows full imaging with a single sophisticated detector unit. Also, since the image is being compressed during the measurement process, CS allows for a fast image acquisition while avoiding any mechanical scan.

THz imaging can also benefit from CS since a heterodyne detector based SPC can show a much better SNR as compared with a direct detector based FPA camera. However, spatial light modulation (SLM) for THz radiation has remained a major bottleneck in the development of THz SPC. In past, different techniques have been used to create spatial masks that can modulate THz wave attenuation in the beam path. The first demonstration of THz SPC was based on metal masks that were constructed and replaced manually [108], resulting in a very slow image acquisition. Since then, other techniques have been used to create reconfigurable masks. In [109] and [110], spatially distributed photo excitation of charge carrier density in a semiconductor wafer was utilized to alter the THz attenuation. In [111], Watts *et al.* report on a THz SPC with an electronically programmable metamaterial mask. However, both of the latter approaches suffer from poor modulation depth ($< 50\%$) that limits the image SNR. These spatial masks also increase the size, complexity, and cost of the imaging setup.

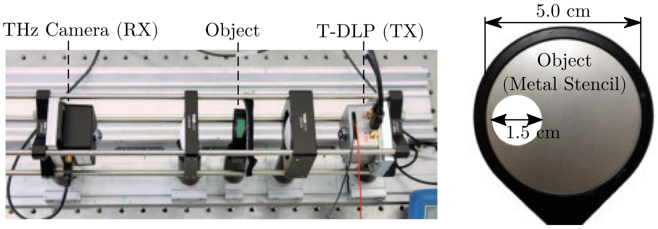

(a) (b)

Fig. 6. THz CS imaging with 4×4 pixel 0.53-THz source array [53] used as T-DLP. (a) Transmission mode imaging setup. (b) Metallic stencil used as a sparse object for imaging experiments.

Mixed-signal integration in silicon technology also allows for novel SLM schemes that can be integrated within the THz source chipset. Such SLM is incorporated in [53], which presents a 4×4 pixel source-array with a TRP of 1 mW at 0.53 THz. Here, an array of incoherent or mutually unlocked free-running oscillators is implemented to destroy source wave coherence and synthesize stochastically independent THz beams for imaging applications [53]. Particularly, each source pixel can be programmed ON or OFF individually through an electronic interface to create SLM at the object plane. Therefore, the source-array module can be used as a THz digital light projector (T-DLP) for SPC without using any external SLM masks. This allows for an infinite modulation depth (effectively limited by the noise-floor of the receiver) and a fast electronic SLM pattern reconfiguration within a scalable T-DLP architecture.

T-DLP-based CS was experimentally investigated with the setup shown in Fig. 6(a). Here, the 4×4 pixel 0.53 THz T-DLP module was used as TX. The 1k-pixel THz camera from [81] was used in power integration mode (equivalent to a single detector unit) as RX for a convenient collection of all source-pixel beams. PTFE lenses with matching f-numbers at the TX and RX were used to create a planar illumination at the object plane and to collect the power at the RX. A metallic stencil with a hole was used as a sparse object, as shown in Fig. 6(b). The object allowed for in-plane rotation to move the position of the hole inside the illumination path. Illumination patterns for SLM were programmed at the source-array module at runtime. For CS imaging, binary low-density parity check matrices were used for close-to-optimal SLM pattern generation on-the-fly with adaptive progressive-edge growth matrix construction in accordance with [112]. To ascertain the reliability of CS-estimated images, individual pixelwise scanned images were also generated. For the latter, each single source-pixel of the of T-DLP was turned ON sequentially and the sampled signals at the RX were recorded. Fig. 7 shows the comparison between image pixel values as scanned sequentially and as estimated with CS methodology, for two different arbitrary object rotations A and B. The bright image pixels are identified correctly in the CS estimation. Here, sequential scanning required 16 measurements for 16 source pixels, whereas CS imaging was performed with only 8 illumination patterns, resulting in a compression ratio of

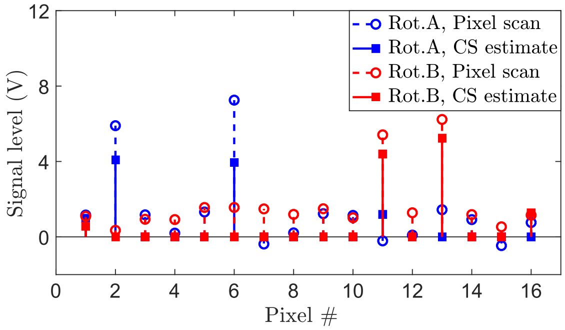

Fig. 7. Comparison of image pixel values (in absolute voltage scale as read out at the RX) obtained from pixelwise sequential scanning and CS estimation, for two arbitrary object rotations A and B. In these measurements, a compression ratio of 50% was achieved with CS imaging.

50% or a twofold speedup in overall measurement time. These initial results indicate the future potential of silicon-integrated source arrays beyond power combining applications, such as for T-DLP-based solid-state compressive imaging in THz, as demonstrated here for the first time.

C. Spectroscopic Imaging

Spectroscopic THz imaging is regarded as one of the key applications for the THz band. Several solid materials exhibit characteristic vibrational phonon modes in the THz frequency band. Thus, THz spectroscopy is envisioned to provide a complementary technique to midinfrared spectroscopy for illegal drugs [113] and explosives [114] detection and is of particular interest for security applications where the specification of solids behind infrared blocker materials is desired. Furthermore, polar gas molecules exhibit quantized rotational resonance states with narrow spectral lines ($\approx$ 1 MHz in the Doppler-limit) in the mmWave-to-THz transition band. Rotational spectroscopy can thus be used for analysis of complex gas mixtures, showing potential for medical diagnosis of the human breath [24], [115].

Established THz spectroscopes operate in time domain (THz-TDS), using femtosecond lasers to generate THz pulses by excitation of nonlinear crystals or photoconductive switches. Commercial THz-TDS systems offer bandwidths of several THz and achieve dynamic range higher than 70 dB. However, they are costly and require bulky auxiliary equipment.

Electronic solutions (silicon and III–V) offer the possibility to implement compact and frequency-agile CW transceivers with sub-kHz frequency resolution. Recent research work on silicon-integrated transceivers for gas spectroscopy has shown that fractional concentration sensitivities as low as a few ppm (without preconcentration) can be identified between 220–320 GHz are achievable with fully integrated silicon implementations [24], [116]. However, THz spectroscopy of condensed matter, e.g., for security applications, requires significantly a higher RF bandwidth, which exceeds the current capabilities of THz integrated electronics. Motivated by the limited RF bandwidth, the functionality of classical frequency-selective THz CW active all-electronic imaging systems was extended in [26] where a multicolor imaging chip-set operating in the 160-to-1000-GHz band was demonstrated in a 0.25-μm SiGe HBT process with $f_T/f_{\max}$ of 280/435 GHz. The imager takes advantage of high-integration levels available by a combination of silicon technologies, very wideband on-chip antenna for THz signal escape, and low-cost chip-on-board (COB) wire-bonded packaging for low-frequency IF and the low-frequency drive for the on-chip LO generation path. It is implemented in the form of two independent single-chip transmitter and receiver modules equipped with the ultrawideband silicon lens-coupled on-chip antennas [117], [118] radiating through the chip backside. Such implementation allows coupling to the quasi-optical train over almost a decade of bandwidth.

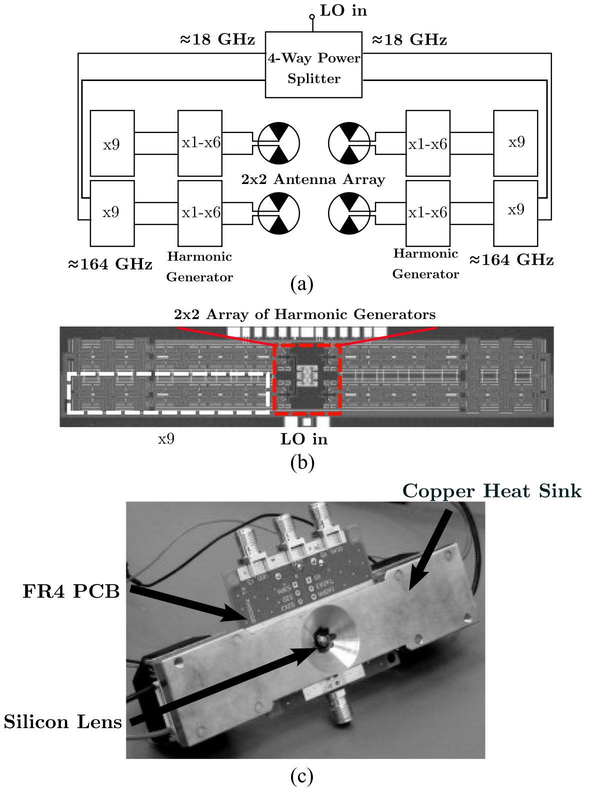

Fig. 8. Transmitter module. (a) Block diagram. (b) Chip micrograph (4.1 × 0.8 mm^2). (c) Packaged module with 4-mm diameter Si-lens; after [26].

The architectures of the receiver and transmitter chips are shown in Figs. 8(a) and 9(a), respectively. They share a common $\times 9$ tunable multiplier chain driven from an external board-level signal located around 17–18 GHz. The $\times 9$-multiplied tone centered around 164 GHz is used to drive either the antenna-coupled harmonic generators on the TX side or the antenna-coupled harmonic mixers on the RX side. The frequency range of 160-to-1000 GHz is not continuously covered with a single frequency multiplication factor but divided into 6 frequency bands that are integer multiples of the fundamental frequency at the $\times 9$ multiplier output. All six harmonics are generated by the harmonic generator circuit of the transmitter module with the power levels sufficient to achieve an appropriately high SNR up to 1 THz. Thereby, six separate THz images can be produced simultaneously for a fixed reference frequency provided to the multiplier chain input. A short performance summary of the multicolor imaging system is given in Table IV.

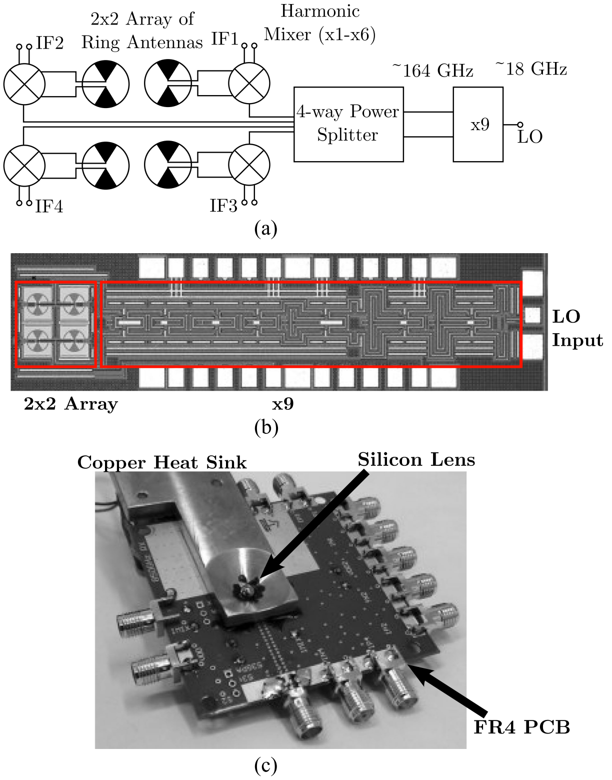

Fig. 9. Receiver module. (a) Block diagram. (b) Chip micrograph (2.2 × 0.6 mm^2). (c) Packaged module with 4-mm diameter Si-lens; after [26].

TABLE IV
MULTICOLOR IMAGING SYSTEM PERFORMANCE SUMMARY

Operation frequency	160-1050 GHz (divided in 6 bands)
Band center frequencies	165, 330, 495, 660, 820, 990 GHz
Peak total radiated power	-37 dBm*to -16 dBm
Noise figure	<48 dB (at 990 GHz)
NEP	<0.24 fW/Hz (at 990 GHz)
System SNR (1 Hz RBW)	70 dB*to 115 dB

* measured including the atmospheric absorption line around 980 GHz; the estimated additional loss is around 10 dB.

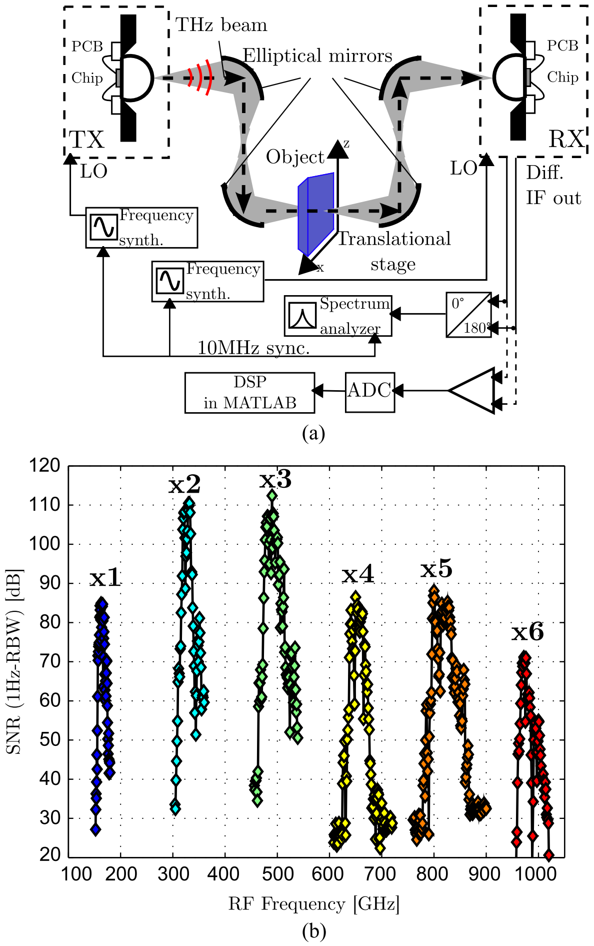

Fig. 10. Transmission-mode imaging setup. (a) Block diagram. (b) SNR (1-Hz RBW) for six harmonic signals of 164 GHz. The free-space propagation path between TX and RX is 150 cm; after [26].

The transmitter and receiver modules were configured into a complete scanning transmission-mode imaging setup, as shown in Fig. 10(a). Here, the diverging beam from the TX module is refocused by two 45° elliptical mirrors (11.3-cm aperture diameter along minor axis and 18.75-cm focal length) onto the object plane. The second set of similar mirrors projects the transmitted signal after passing the object onto the receiver module plane. For this particular setup, the SNR within 1-Hz resolution bandwidth was measured to be 90 dB for the 165 GHz band, 115 dB for the 330 and 495 GHz bands, 95 dB for the 660 and 820 GHz band, and 70 dB for the 990 GHz band [see Fig. 10(b)].

The optical quality in the imaging setup was investigated with the knife-edge approach. The evolution of the beam size along the beam propagation path (z-axis) around the image plane for all six harmonic signals altogether with the fitting hyperbolas to the fundamental Gaussian mode is presented in Fig. 11(a). The measured beam waist varies between 2.2 mm for 160 GHz down to around 0.8 mm for higher order harmonics whereas the location of beam waist (along z-axis) varies by no more than 3 mm and stays within a depth of focus for all harmonic tones (7–18 mm). The lateral resolution of the setup was further verified with a resolution target located in the imaging plane. As a resolution target, a thin laminate board with the etched copper structures with varying feature size was applied [see Fig. 11(b)]. Two exemplary chosen THz images of the target at 492 GHz and 984 GHz are shown in Fig. 11(c). The features around 1 mm in size can be still resolved, correlating well with the previously estimated beam spot size. Both images are normalized to the maximum received power for each frequency band separately.

Fig. 12 shows six multicolor images of some sweets. The applied color scale for each of the images is normalized to the maximum received signal level in each harmonic. The image was acquired with a scanning speed of 40 pixels/s with a 0.5-mm step size and with an equivalent noise bandwidth (ENBW) of 366 Hz. This noise bandwidth corresponds to a 25.6-dB reduction of the image SNR when compared to that from Fig. 10 for a 1-Hz bandwidth. The effective SNR achieved for each of the harmonic subfigures is denoted in Fig. 12(b).

The images show a distinct frequency-dependent material absorption for different sweet types. It is interesting to notice that

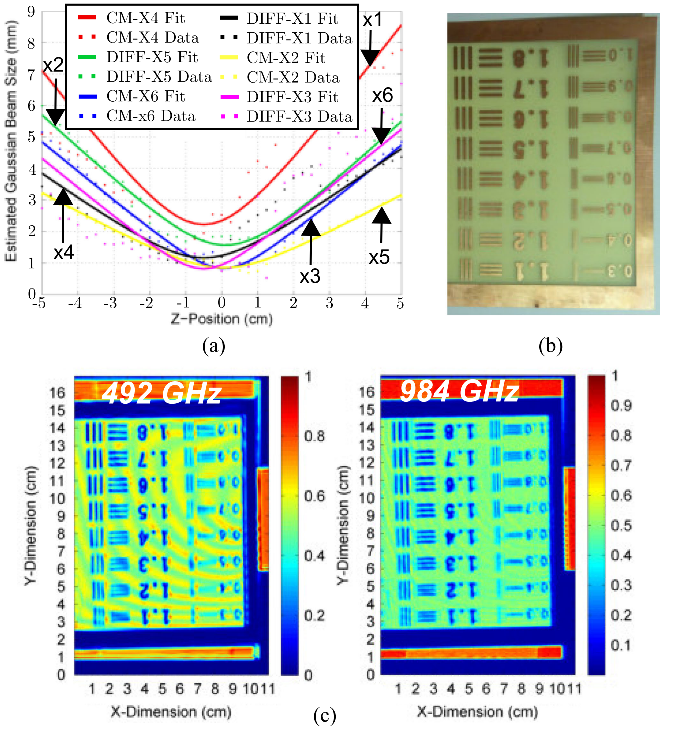

Fig. 11. Optical quality of the imaging setup. (a) Evolution of the beam size around the image plane for all six harmonic bands. (b) Resolution target with the indicated feature size in mm. (c) 492- and 984-GHz spectral image of the target in the linear scale. Each of the images is normalized to its own received peak power.

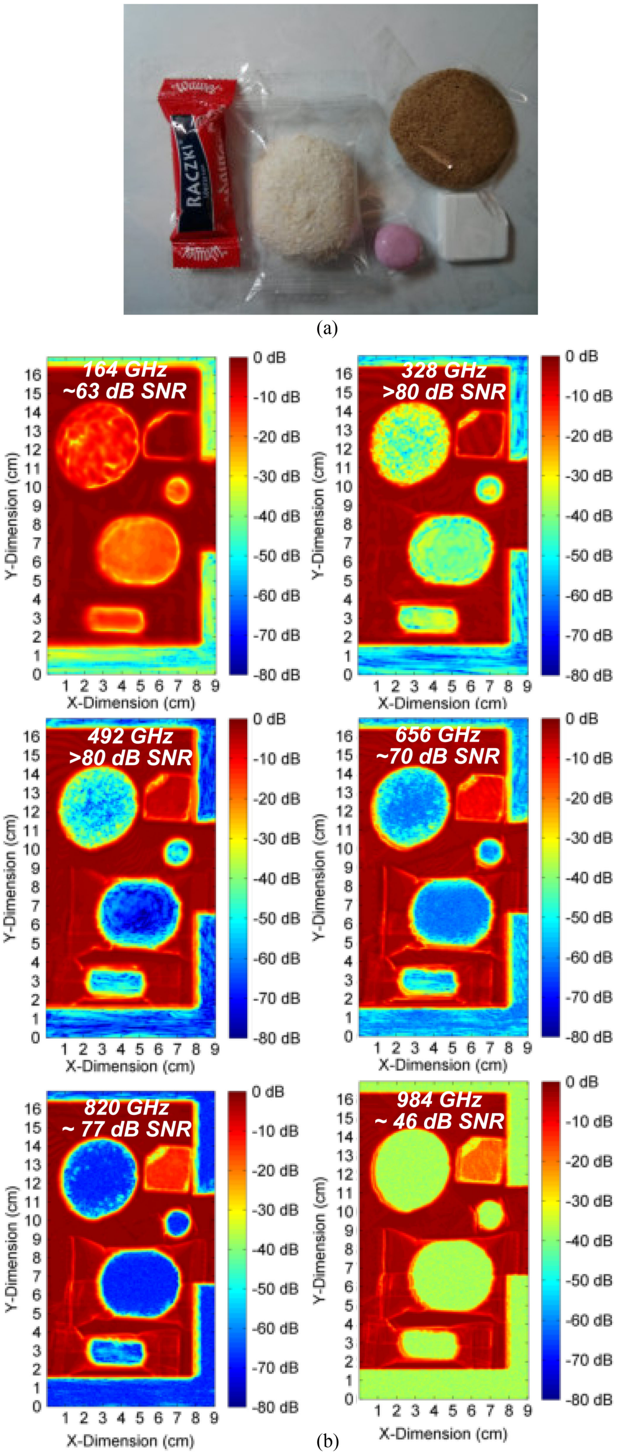

Fig. 12. Multicolor transmission-mode THz image of sweets. (a) Photograph of the imaged object. (b) Spectral images with indicated SNR for each harmonic band. All plots share the same scale of 80 dB but are normalized to their maximum received power levels.

the transparent plastic foil cover for some of the packaged sweets starts to be well visible for higher harmonics, indicating the usefulness of the multicolor imaging technique for enhancing the object detection probability.

D. FMCW Radar Imaging

In contrast to other previously discussed active imaging techniques, radars can enhance the image quality in reflection-mode as they provide range-gating capabilities. Therefore, THz radars may be used for inspection of packages with reflecting surfaces [42] or high-precision remote gesture recognition [8]. Similar to other general-purpose transceivers in the upper mmWave and THz bands, radar imagers typically rely on multidie split-block waveguide assemblies and, therefore, show low integration levels [119], [120], [121].

To respond to the needs of the future radar sensors in high-volume consumer and industrial markets [122], [123], a high-resolution single-chip FMCW monostatic homodyne radar front-end module operating around 210–270 GHz [42] was developed in 130-nm SiGe HBT technology with $f_t/f_{\max}$ of 300/500 GHz [32]. A COB packaging scheme with a broadband silicon lens-integrated on-chip slot antenna [124], [125] for THz signal escape (see Fig. 13) was implemented. Contrary to other highly integrated linearly polarized monostatic radars, here presented radar employs circular polarization to isolate transmitter and receiver paths connected to a single antenna that results in a 6-dB improvement in SNR [126], [127]. The other possible advantages of this solution are the reduction of the influence of ghost targets in indoor environments, reduced sensitivity to wave depolarization effects or receiver jamming for multisensor operation [128].

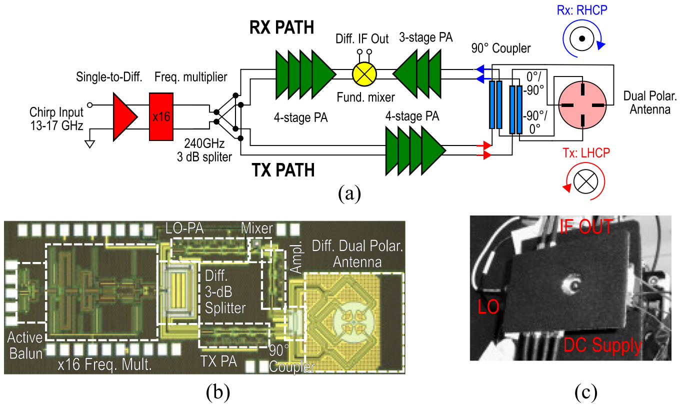

(a)

(b)

(c)

Fig. 13. 210–270 GHz radar front-end chip in 0.13-μm SiGe HBT technology. (a) Chip architecture. (b) Chip micrograph; after [42]. (c) Silicon lens-packaged radar module on low-cost FR-4 PCB with the mounted absorber material. The chip size is $2.9 \times 11\ \text{mm}^2$, whereas the lens diameter is 9 mm.

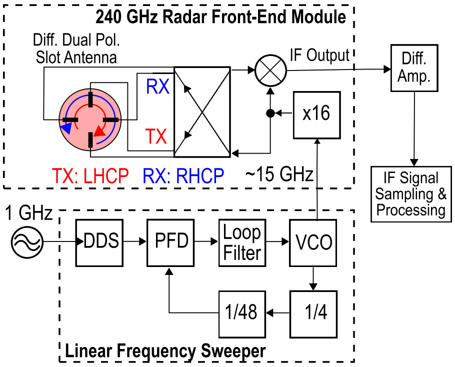

Fig. 14. Complete FMCW radar system. The system comprises the 240-GHz transceiver module, an in-house developed linear frequency-sweep generator, an external ADC for IF signal sampling and MATLAB-based data-processing tool.

TABLE V
240-GHz RADAR SYSTEM PERFORMANCE SUMMARY

Center RF frequency	240 GHz (15 GHz $\times$ 16)
Peak total radiated power	+5 dBm
Noise figure	21 dB (with TX running)
Antenna directivity	25.8–27.8 dB (210-270 GHz)
Sweep bandwidth	60 GHz
Range resolution	2.57 mm (theoretical: 2.5 mm)
Sweep time	100 µm-2 ms
RMS ramp-linearity	9 kHz (60 GHz sweep in 2 ms)
Total jitter of the ramp generator	2.62° (10 Hz–100 MHz)
Spurious-free dynamic range	≈40 dB
Power dissipation	1.6 W

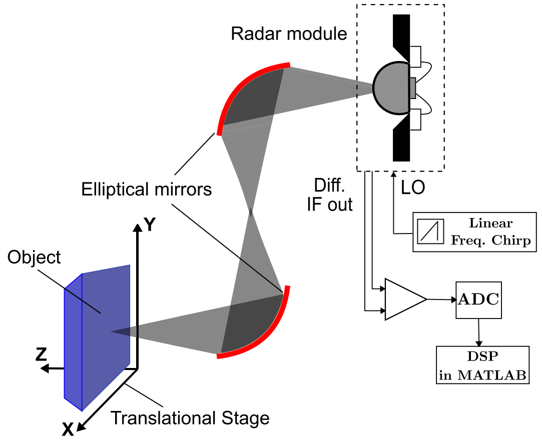

Fig. 15. Reflection-mode scanning setup with the radar module; after [42]. The same set of elliptical mirrors to that from the multicolor imaging experiment was applied. The free-space propagation path between the radar module and the imaged object is around 78 cm.

The radar chip employs a wideband LO-generation path based on a multiplier-chain architecture with $\times 16$ multiplication factor applied to an external linear-frequency chirp signal around 13–17 GHz (see Fig. 13) provided on-board from a sawtooth frequency-ramp generator. The output signal from the multiplier-chain after 3-dB split and power amplification by two four-stage PAs with small-signal gain of 14 dB and P_{sat} of 7 dBm [129] drives both the transmitter input of the circularly polarized antenna and the fundamentally operated Gilbert-cell based downconversion mixer. The RF port of the mixer is preceded by a three-stage power amplifier instead of regular LNA for improved bandwidth and linearity [42]. Circular polarization in a broad frequency range is realized by the combination of a wideband quadrature coupler [124] with a broadband annular-slot antenna supporting two orthogonal polarizations [124], [125]. The frequency-dependent directivity of the radar module packed with a 9-mm diameter silicon hyperhemispherical lens was measured to be 25.8–27.8 dB and 25.9–27 dB in 210–270 GHz for the transmitter and receiver mode of operation, respectively. The measured peak TRP from the fully packaged radar module is $+5$ dBm with the corresponding noise figure of 21 dB in the presence of the transmitter leakage running simultaneously. The RF front-end was further extended by an in-house developed linear-frequency saw-tooth chirp generator and a data acquisition unit with MATLAB code for signal processing (see Fig. 14).

The calibrated radar response is currently influenced by $\times 14$ and $\times 18$ parasitic harmonic spurs from the multiplier chain based LO generation path, which limit both the spurious-free dynamic range (SFDR) and the ramp operational RF bandwidth to around 60 GHz: 15 GHz $(\times 18 - \times 14) = 60$ GHz for the center ramp frequency of 15 GHz. A close-to-theoretical range-resolution of 2.57 mm was extracted from the main-lobe full-width at -6 dB of the point-spread function (PSF) of the calibrated beat signal spectrum for the maximum supported 60 GHz ramp swept over 2 ms. A brief performance summary of the radar system is provided in Table V.

To demonstrate the performance of the complete radar system, a reflection-mode scanning setup (see Fig. 15) was assembled with the same set of elliptical mirrors to that from the multicolor imaging experiment. A 16-b ADC card with the sampling rate of 3 MHz digitized the time-domain trains of the IF beat signals after differential preamplification. For FFT data postprocessing, a Hamming window was applied as a good compromise between selectivity and resolution (maximum side-lobe level of -43 dB, -6 dB main-lobe width of 1.81 [130]). In combination with a 60-GHz bandwidth swept in 2 ms (4000 samples), it results in an equivalent noise bandwidth of 680 Hz and a main-lobe

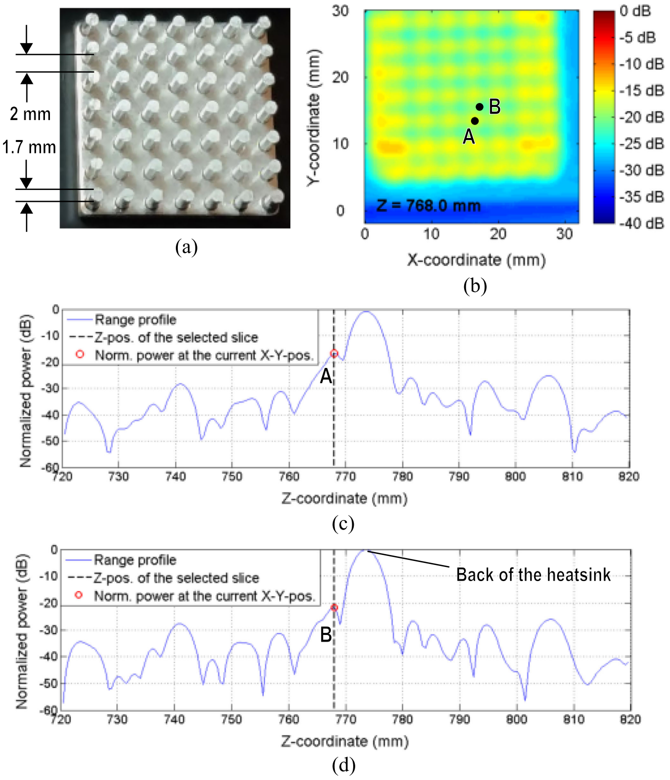

(a) (b) (c) (d)

Fig. 16. Radar imaging experiment with an aluminum pin-type heat sink as a resolution target. (a) Photograph of the heat sink with indicated lateral dimensions. The pin height is around 5 mm. (b) 2-D image of the normalized receiver power for the object-to-radar distance corresponding to the top of the pins (768 mm). (c) and (d) Range profiles for two selected positions marked with dots. Position A denotes the pin location, whereas B corresponds to the free-space between two pins. The range profiles were sampled at a 0.5-mm spacing.

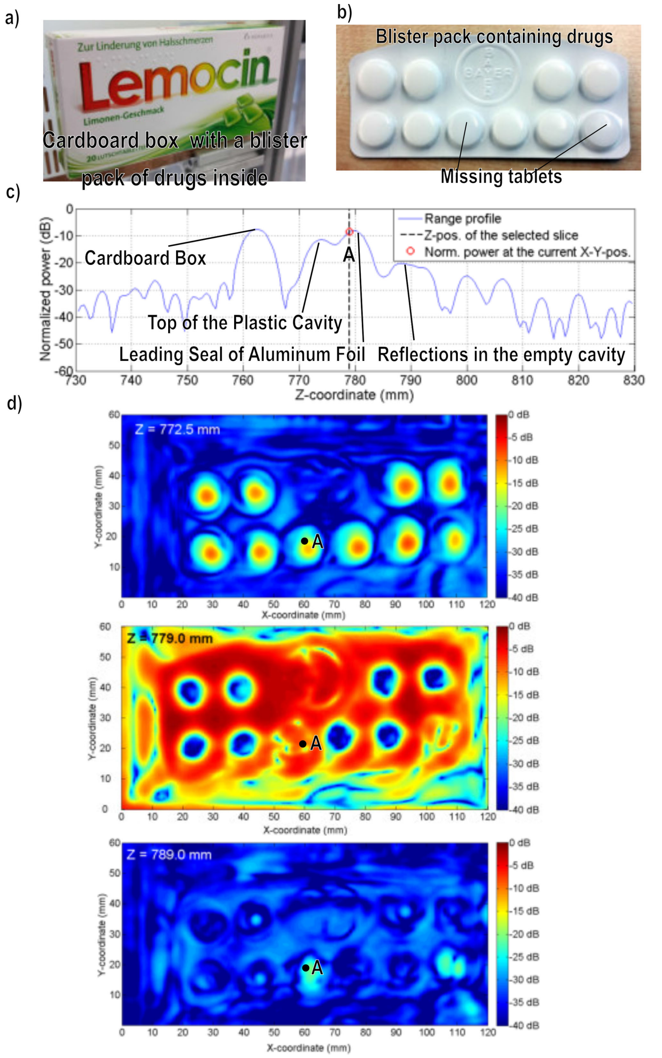

Fig. 17. Radar imaging of a blister pack of drugs hidden in a cardboard box; after [42]. Two tablets are missing. (a) and (b) Visible-light photos of the box and the blister pack, respectively. (c) Range profile for a single position A across the cardboard box corresponding to a missing tablet in the center. (d) 2-D images of the normalized receiver power for three different distances to the radar module. A distance of 772.5 mm is aligned with the top of the plastic cavity, whereas 779 mm matched an aluminum foil sealing the back of the cavity. Multiple reflections in the empty cavity are primarily responsible for the radar echo for larger distances (e.g., 789 mm). The acquired range profiles show a dynamic range of around 48 dB.

full width at −6 dB of around 4.65 mm. In the first imaging experiment (see Fig. 16), an aluminum pin-type heatsink was used as a scanned target to verify both the cross range as well as the lateral resolution of the complete setup. Each of the pins is around 5-mm high and is considered to be an object feature with low radar cross section compared to a large backside of the heatsink in its close proximity and in the range of expected radar cross-range resolution. From the provided 2-D image of the normalized received power at the top of the pins and the range profiles for two selected positions across the heatsink, one can notice that the 1.7-mm diameter and 5-mm high pins can be appropriately resolved. Another imaging experiment was conducted with a blister pack of drugs hidden in a cardboard box with the goal to be able to detect two missing tablets. Exemplary, the chosen range profile for a single position (*XY*) across the cardboard corresponding to the missing tablet altogether with three different 2-D images of the normalized received power for selected distances along this profile are depicted in Fig. 17. Please note that from the first 2-D image at a distance of 772.5 mm corresponding to the top of the plastic cavity, the missing tablet cannot be resolved, whereas the next profile only 6 mm behind and located around the leading seal of aluminum foil allows identification of the missing tablet, thanks to the provided radar cross-range resolution. From the last profile (789 mm), multiple reflections only in the empty cavities for two missing tablets generate nonphysical return signals at distances behind the backside of an aluminum foil. In Fig. 18, a 3-D surface-reconstructed picture of the blister pack is shown, which was created with a simple peak-search algorithm to identify the range position of the feature with the highest reflected power for each lateral (*XY*) position across the scanned object. To allow identification of the missing tablets, the data were here range-gated appropriately to discard the influence of the masking reflections in front of and behind the tablets.

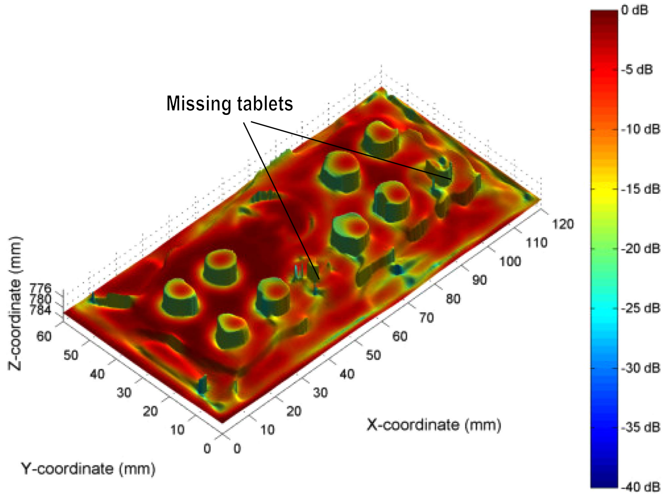

Fig. 18. 3-D surface reconstruction of the blister packs with two tablets missing with a peak-searching algorithm; after [42]. The data were range-gated appropriately to remove the influence of multipath reflections behind the tablets as well as reflections from the front side of the cardboard box and the plastic cavities. The image color scale represents the normalized received power.

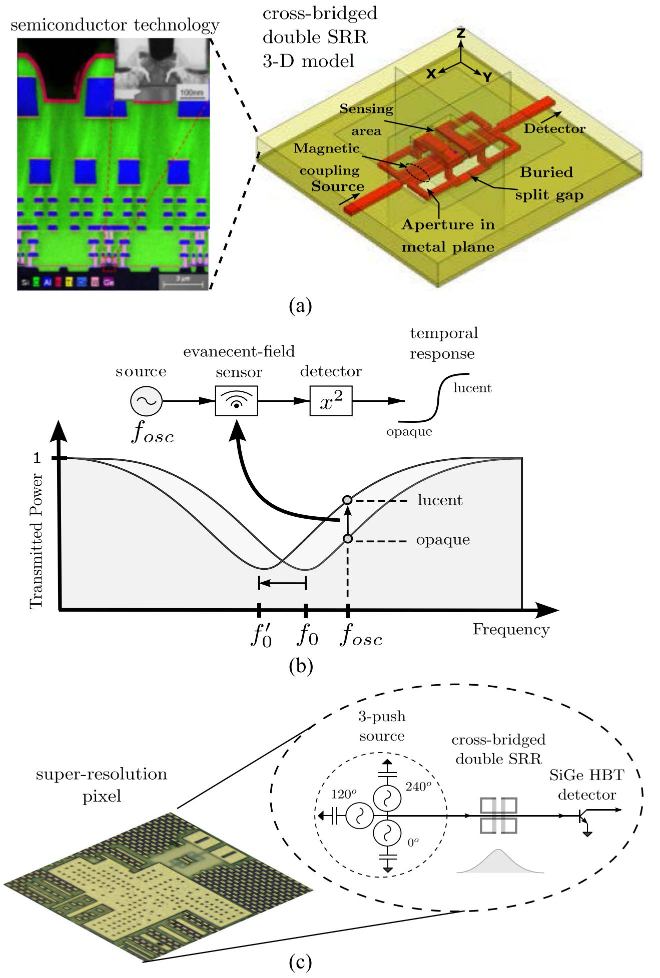

Fig. 19. Single-ended silicon-integrated subwavelength THz sensor; after [86]. (a) 3-D illustration of the cross-bridged double split-ring-resonator embedded into a 3-D multilayer silicon-dioxide stack on top of a silicon substrate. A SEM view of the used technology cross-section is also shown. (b) Incoherent operation mode based on measurement of the temporal power transmission changes across the resonant curve. (c) Micrograph of the implemented imaging device with cascaded source, resonator, and power detector components indicated.

E. Near-Field Imaging

The spatial resolution THz far-field imaging is fundamentally restricted by Abbe's diffraction limit, which is in the mm-range at THz frequencies. This can be far too low for many promising THz applications, e.g., semiconductor process quality control [131] and *in situ* assessment of malignant tissue margins during segmental mastectomy breast cancer surgeries [10]. In the last decades, there has thus been a significant interest in THz near fields which can interact with micro- and nanoscale phenomenon. Today's common THz near-field imaging systems rely on near-field scanning optical microscopy (NSOM). Here, metallic or optically gated apertures, scattering probe-tips, or electro-optical probes [132]–[135] are illuminated with THz radiation to achieve subwavelength resolution. The typical resolution of such systems is in the micrometer range [135], whereas record resolution of 20–40 nm has also been demonstrated with atomic-force microscopy tips [134]. Yet, in a majority of such systems, either the illumination or the detection paths are placed remotely, resulting in weakly detected signals additionally shadowed by strong far-field background clutter. Even with high-power sources and cooled detectors [132]–[134], [136], [137] long integration times are needed for reasonable sensitivity, making real-time visualization very challenging.

The implementation of THz near-field sensing in integrated electronics can solve some of the major issues undermining classical THz NSOM methods. In particular, integrated circuits allow cointegration of superresolution near-field probe, illumination source, and detector on the same die, which can mitigate the sensitivity problems associated with remote component placement. Furthermore, silicon technology facilitates the multipixel integration of near-field sensors, which can reduce required scanning times or obviate the need for scanning in general. Silicon integrated terahertz superresolution sensors have been reported in [22], [29], and [86]. Here, one major implementation challenge is building a highly confined subwavelength near-field probe in a planar technology, which is difficult in view of the thin, electrically small dielectric stack. The idea applied in [22], [29], and [86] is to measure the resonant shift of a split-ring-resonator (SRR) upon loading it with a sample. Thereby, only the field of the electric-dipole-type field of the split-gap is exposed to the chip top surface and the sensors rely on capacitive near-field coupling with an object. To minimize the effective size of the sensing surface, a 3-D SRR topography is embedded in the multilayer BEOL, as shown in Fig. 19(a). The achieved lateral resolution with this approach is 10–15 μm at 530 GHz [29], [86].

Another challenge arises from operation at THz frequencies, which restricts potential circuit architectures for sensor illumination and detection to very low complexity. Thus, the sensors pursue an entirely incoherent sensing concept where the SRR is illuminated by a free-running on-chip oscillator and the transmitted power through the SRR is detected with a broadband

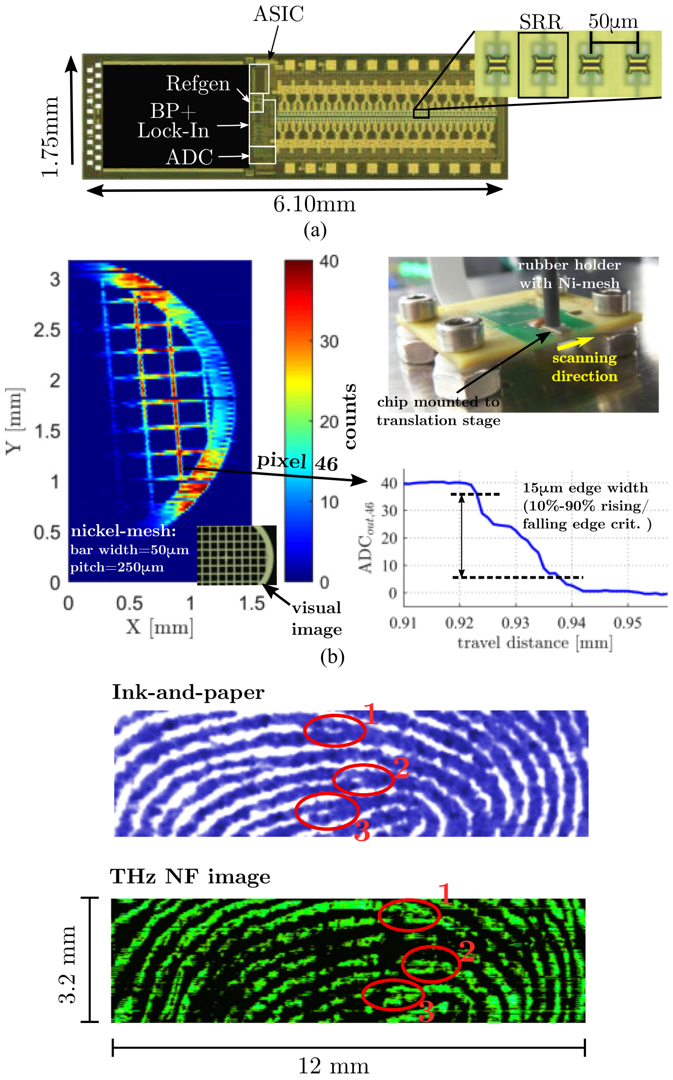

(c)

Fig. 20. 128-pixel near-field sensor system-on-a-chip; after [29]. (a) Chip micrograph. (b) Imaging results and setup for a 1-D scan of a nickel-mesh. (Image size $= 1500 \times 128$ pixels, step size $= 1\mu$m, $T_{\rm scan} = 6$ min 45 s, frame rate = 6 fps). (c) Imaging results for a 1-D scan of a human fingerprint; after [138]. (Image size $= 842 \times 128$ pixels, $T_{\rm scan} = 30$ s, frame rate $= 15$ fps).

SiGe HBT power detector, as shown in Fig. 19(b). Detection of the frequency shift is translated to measuring the differential temporal transmission changes from opaque to lucent at the detector output for the operation frequency set by the illumination source. Note that while more complex architectures, such as an integrated heterodyne detector, may provide a better sensitivity, they are avoided to facilitate multipixel integration and low dc power consumption.

The massive multipixel integration of near-field sensors is still limited in terms of sensor pitch due to the on-chip oscillators, which require wavelength-size passive tuning elements introducing an elemental size difference between the SRR and the oscillator, as shown in Fig. 19(c). Thus, a circuit architecture based on power distribution networks was pursued in [29] to achieve a high pixel density in a 1-D array. The THz wave generated by a single oscillator is fanned out to four SRRs, spaced at a 50-μm pitch. With further vertical mirroring, a 25-μm pixel pitch and a 1-D fill factor of 48% corresponding to a density of around 100 ppi was achieved. This concept was applied to build a 550 GHz 128 pixel near-field sensing system-on-a-chip (SoC) with cointegrated mixed-signal baseband signal processing in 0.13-μm SiGe BiCMOS technology [29]. Fig. 20(a) shows the micrograph of the SoC. It implements a large-scale detector read-out scheme with an integrated lock-in circuitry and subsequent 6-bit digitization, achieving a DR of 37 dB at a frame rate of 28 fps. Table VI summarizes the most important performance metrics of the SoC.

TABLE VI
NEAR-FIELD ARRAY PERFORMANCE SUMMARY

Operation frequency	534–562 GHz
Number of pixels	128
Dynamic range	37 dB*
Resolution	10–15 µm
Scanning speed	280 µs/pix

* For a digital real-time readout with 28 fps frame rate.

Two imaging experiments were conducted with the sensor array. First, a nickel-mesh with a 50-μm bar width and a 250-μm bar pitch was scanned with a 1-D translation of the SoC. The corresponding THz near-field image, as shown in Fig. 20(b), clearly depicts the subwavelength-sized features of the mesh. In the second experiment, biometrical human fingerprint reading was demonstrated with the SoC [138]. Here, a finger was moved orthogonally across the sensor surface. The results of the fingerprint acquisition are shown in Fig. 20(c). The high integration level and the ability of high-speed room-temperature operation are a good starting point for further research on fully integrated, large-count arrays of superresolution THz sensors. Future directions in this field may thus include research on implementation of dense 2-D arrays, measurement bandwidth extension, or sensor calibration.

IV. CONCLUSIONS AND OUTLOOK

In this paper, it was demonstrated that silicon-based THz ICs show potential to leverage various THz imaging and sensing applications. THz IC design has recently emerged into a vibrant field of research, achieving breakthroughs in practical utility, potential system cost, and integration level of THz components—the frontiers that constitute the bottleneck for adoption and commercialization of THz technology. In particular, this paper demonstrates that the research in THz ICs has enabled the cost-effective realization of THz applications, such as tomographic imaging, multicolor imaging, high-resolution radar imaging, near-field imaging, and CS.

This paper identifies two major driving forces behind THz IC advances. First, the power generation capability of THz ICs is tightly coupled to the progress in silicon technology. Present foundry-level SiGe HBT technology is just on the verge of enabling fundamental circuit operation in the lower part of the THz band, and it continues to show a great development potential regarding device speed with predicted $f_{\max}$ beyond 1 THz [6].

Therefore, SiGe BiCMOS technology may transpire as the predominant technology platform for low-cost THz components. Second, advances in THz IC technology are driven by the invention of novel circuit and system architectures that exploit the massive scalability and design space of silicon technology. THz IC designers are confronted with an interdisciplinary set of challenges on the device, electromagnetic design, and packaging levels that cannot be overcome by the transfer of classic millimeter-wave design techniques to the THz band.

This paper furthermore highlights that a new generation of THz on-chip systems (SoCs) promises to extend the functional scope of THz imaging systems [29], [30]. For example, the mixed-signal reconfigurability of THz SoCs may enable rapid spatial illumination control [36], [53], [62] for compressed sensing, communication, and light-field applications [28], or built-in calibration of large-scale detector arrays [81], [29]. Therefore, THz ICs should not only be seen as a compact, low-cost, and inferior alternative to traditional THz equipment, but as an enabler for new imaging modalities, opening up new applications and markets.

REFERENCES

[1] C. Kulesa, “Terahertz spectroscopy for astronomy: From comets to cosmology,” *IEEE Trans. THz Sci. Technol.*, vol. 1, no. 1, pp. 232–240, Sep. 2011, doi: 10.1109/TTHZ.2011.2159648.

[2] I. Mehdi, J. V. Siles, C. Lee, and E. Schlecht, “THz diode technology: Status, prospects, and applications,” *Proc. IEEE*, vol. 105, no. 6, pp. 990–1007, Jun. 2017, doi: 10.1109/JPROC.2017.2650235.

[3] H. Hübers, “Terahertz heterodyne receivers,” *IEEE J. Sel. Topics Quantum Electron.*, vol. 14, no. 2, pp. 378–391, Mar. 2008, doi: 10.1109/JSTQE.2007.913964.

[4] A. Maestrini *et al.*, “Schottky diode-based terahertz frequency multipliers and mixers,” *Comptes Rendus Physique*, vol. 11, no. 7–8, pp. 480–495, Oct. 2010.

[5] A. L. Betz and R. T. Boreiko, Far-infrared heterodyne spectrometer for SOFIA, Center Astrophys. Space Astron., Colorado Univ.; Boulder, CO, USA, Tech. Rep. NASA Grant NAG 2-1062, Jan. 1998.

[6] M. Schröter *et al.*, “SiGe HBT technology: Future trends and TCAD-based roadmap,” *Proc. IEEE*, vol. 105, no. 6, pp. 1068–1086, Jun. 2017, doi: 10.1109/JPROC.2015.2500024.

[7] P. Rodriguez-Vazquez, J. Grzyb, N. Sarmah, B. Heinemann, and U. R. Pfeiffer, “A 65 Gbps QPSK one meter wireless link operating at a 225–255 GHz tunable carrier in a SiGe HBT technology,” in *Proc. IEEE Radio Wireless Symp.*, Anaheim, CA, USA, 2018, pp. 146–149, doi: 10.1109/RWS.2018.8304970.

[8] J. Lien *et al.*, “Soli,” *ACM Trans. Graph.*, vol. 35, no. 4, pp. 1–19, Jul. 2016, doi: 10.1145/2897824.2925953.

[9] D. Zimdars and J. S. White, “Terahertz reflection imaging for package and personnel inspection,” *Proc. SPIE*, vol. 5411, pp. 78–84, Sep. 2004, doi: 10.1117/12.562216.

[10] Q. Cassar *et al.*, “Pilot study of freshly excised breast tissue response in the 300–600 GHz range,” *Biomed. Opt. Express*, vol. 9, no. 7, pp. 2930–2942, Jun. 2018, doi: 10.1364/BOE.9.002930.

[11] T. W. Crowe, J. L. Hesler, S. A. Retzloff, and D. S. Kurtz, “Higher power multipliers for terahertz sources,” in *Proc. 41st Int. Conf. Infrared, Millim., THz Waves*, Copenhagen, Denmark, Sep. 2016, p. 1, doi: 10.1109/IRMMW-THz.2016.7758351.

[12] X. Mei *et al.*, “First demonstration of amplification at 1 THz using 25-nm InP high electron mobility transistor process,” *IEEE Electron Device Lett.*, vol. 36, no. 4, pp. 327–329, Apr. 2015, doi: 10.1109/LED.2015.2407193.

[13] E. N. Grossman, K. Leong, X. Mei, and W. Deal, “Low-frequency noise and passive imaging with 670 GHz HEMT low-noise amplifiers,” *IEEE Trans. THz Sci. Technol.*, vol. 4, no. 6, pp. 749–752, Nov. 2014, doi: 10.1109/TTHZ.2014.2352035.

[14] J. J. Lynch *et al.*, “Passive millimeter-wave imaging module with preamplified zero-bias detection,” *IEEE Trans. Microw. Theory Techn.*, vol. 56, no. 7, pp. 1592–1600, Jul. 2008, doi: 10.1109/TMTT.2008.924361.

[15] A. Timofeev *et al.*, “Optical and electrical characterization of a large kinetic inductance bolometer focal plane array,” *IEEE Trans. THz Sci. Technol.*, vol. 7, no. 2, pp. 218–224, Mar. 2017, doi: 10.1109/TTHZ.2016.2639470.

[16] K. B. Cooper, R. J. Dengler, N. Llombart, B. Thomas, G. Chattopadhyay, and P. H. Siegel, “THz imaging radar for standoff personnel screening,” *IEEE Trans. THz Sci. Technol.*, vol. 1, no. 1, pp. 169–182, Sep. 2011, doi: 10.1109/TTHZ.2011.2159556.

[17] S.-P. Han *et al.*, “Real-time continuous-wave terahertz line scanner based on a compact 1×240 InGaAs Schottky barrier diode array detector,” *Opt. Express*, vol. 22, no. 23, pp. 28977–28983, Nov. 2014, doi: 10.1364/OE.22.028977.

[18] R. Al Hadi *et al.*, “A broadband 0.6 to 1 THz CMOS imaging detector with an integrated lens,” in *Proc. IEEE MTT-S Int. Microw. Symp.*, Jun. 2011, pp. 1–4, doi: 10.1109/MWSYM.2011.5972870.

[19] N. Palka, M. Szala, and E. Czerwinska, “Characterization of prospective explosive materials using terahertz time-domain spectroscopy,” *Appl. Opt.*, vol. 55, no. 17, pp. 4575–4583, Jun. 2016, doi: 10.1364/AO.55.004575.

[20] T. Bowman, M. El-Shenawee, and L. K. Campbell, “Terahertz transmission vs reflection imaging and model-based characterization for excised breast carcinomas,” *Biomed. Opt. Express*, vol. 7, no. 9, pp. 3756–3783, Sep. 2016, doi: 10.1364/BOE.7.003756.

[21] L. Li *et al.*, “Terahertz quantum cascade lasers with > 1 W output powers,” *Electron. Lett.*, vol. 50, no. 4, pp. 309–311, Feb. 2014, doi: 10.1049/el.2013.4035.

[22] J. Grzyb, B. Heinemann, and U. R. Pfeiffer, “A 0.55 THz near-field sensor with a μm-range lateral resolution fully integrated in 130 nm SiGe BiCMOS,” *IEEE J. Solid-State Circuits*, vol. 51, no. 12, pp. 3063–3077, Dec. 2016, doi: 10.1109/JSSC.2016.2603992.

[23] D. Wang *et al.*, “Integrated 240-GHz dielectric sensor with dc readout circuit in a 130-nm SiGe BiCMOS technology,” *IEEE Trans. Microw. Theory Techn.*, vol. 66, no. 9, pp. 4232–4241, Sep. 2018, doi: 10.1109/TMTT.2018.2839104.

[24] C. Wang, B. Perkins, Z. Wang, and R. Han, “Molecular detection for unconcentrated gas with PPM sensitivity using 220-to-320-GHz dual-frequency-comb spectrometer in CMOS,” *IEEE Trans. Biomed. Circuits Syst.*, vol. 12, no. 3, pp. 709–721, Jun. 2018, doi: 10.1109/TBCAS.2018.2812818.

[25] P. Hillger, A. Schlter, R. Jain, S. Malz, J. Grzyb, and U. Pfeiffer, “Low-cost 0.5 THz computed tomography based on silicon components,” in *Proc. 42nd Int. Conf. Infrared, Millim., THz Waves*, Cancun, Mexico, Aug. 2017, pp. 1–2, doi: 10.1109/IRMMW-THz.2017.8067136.

[26] K. Statnikov, J. Grzyb, B. Heinemann, and U. R. Pfeiffer, “160-GHz to 1-THz multi-color active imaging with a lens-coupled SiGe HBT chip-set,” *IEEE Trans. THz Sci. Technol.*, vol. 63, no. 2, pp. 520–532, Feb. 2015, doi: 10.1109/TMTT.2014.2385777.

[27] N. Weimann *et al.*, “Tight focus toward the future: Tight material combination for millimeter-wave RF power applications: InP HBT SiGe BiCMOS heterogeneous wafer-level integration,” *IEEE Microw. Mag.*, vol. 18, no. 2, pp. 74–82, Mar. 2017, doi: 10.1109/MMM.2016.2635859.

[28] R. Jain, J. Grzyb, and U. R. Pfeiffer, “Terahertz light-field imaging,” *IEEE Trans. THz Sci. Technol.*, vol. 6, no. 5, pp. 649–657, Sep. 2016, doi: 10.1109/TTHZ.2016.2584861.

[29] P. Hillger *et al.*, “A 128-pixel 0.56 THz sensing array for real-time near-field imaging in 0.13 μm SiGe BiCMOS,” in *Proc. IEEE Int. Solid-State Circuits Conf.*, San Francisco, CA, USA, Feb. 2018, pp. 418–420, doi: 10.1109/ISSCC.2018.8310362.

[30] X. Wu and K. Sengupta, “On-chip THz spectroscope exploiting electromagnetic scattering with multi-port antenna,” *IEEE J. Solid-State Circuits*, vol. 51, no. 12, pp. 3049–3062, Dec. 2016, doi: 10.1109/JSSC.2016.2597845.

[31] J. Grzyb and U. Pfeiffer, “THz direct detector and heterodyne receiver arrays in silicon nanoscale technologies,” *J. Infrared, Millim., THz Waves*, vol. 36, no. 10, pp. 998–1032, Oct. 2015, doi: 10.1007/s10762-015-0172-6.

[32] B. Heinemann *et al.*, “SiGe HBT technology with $f_T/f_{\max}$ of 300 GHz/500 GHz and 2.0 ps CML gate delay,” in *IEEE Int. Electron Devices Meeting*, San Francisco, CA, USA, Dec. 2010, pp. 30.5.1–30.5.4, doi: 10.1109/IEDM.2010.5703452.

[33] S. Emami *et al.*, “A 60 GHz CMOS phased-array transceiver pair for multi-Gb/s wireless communications,” in *Proc. IEEE Int. Solid-State Circuits Conf.*, San Francisco, CA, USA, 2011, pp. 164–166, doi: 10.1109/ISSCC.2011.5746265.

[34] H. P. Forstner *et al.*, “A 77 GHz 4-channel automotive radar transceiver in SiGe,” in *Proc. IEEE Radio Freq. Integr. Circuits Symp.*, Atlanta, GA, USA, Jun. 2008, pp. 233–236, doi: 10.1109/RFIC.2008.4561425.

[35] K. Sengupta and A. Hajimiri, “A 0.28 THz power-generation and beam-steering array in CMOS based on distributed active radiators,” *IEEE J. Solid-State Circuits*, vol. 47, no. 12, pp. 3013–3031, Dec. 2012, doi: 10.1109/JSSC.2012.2217831.

[36] Y. Tousi and E. Afshari, “A high-power and scalable 2-D phased array for terahertz CMOS integrated systems,” *IEEE J. Solid-State Circuits*, vol. 50, no. 2, pp. 597–609, Feb. 2015, doi: 10.1109/JSSC.2014.2375324.

[37] R. Han *et al.*, “A SiGe terahertz heterodyne imaging transmitter with 3.3 mW radiated power and fully-integrated phase-locked loop,” *IEEE J. Solid-State Circuits*, vol. 50, no. 12, pp. 2935–2947, Sep. 2015, doi: 10.1109/JSSC.2015.2471847.

[38] H. Jalili and O. Momeni, “A 0.34-THz varactor-less scalable standing wave radiator array with 5.9% tuning range in 130 nm BiCMOS,” in *Proc. IEEE Radio Freq. Integr. Circuits Symp.*, San Francisco, CA, USA, May 2016, pp. 182–185, doi: 10.1109/RFIC.2016.7508281.

[39] Z. Hu, M. Kaynak, and R. Han, “High-power radiation at 1 THz in silicon: A fully scalable array using a multi-functional radiating mesh structure,” *IEEE J. Solid-State Circuits*, vol. 53, no. 5, pp. 1313–1327, May 2018, doi: 10.1109/JSSC.2017.2786682.

[40] S. P. Voinigescu *et al.*, “A study of SiGe HBT signal sources in the 220–330-GHz range,” *IEEE J. Solid-State Circuits*, vol. 48, no. 9, pp. 2011–2021, Sep. 2013, doi: 10.1109/JSSC.2013.2265494.

[41] B. Heinemann *et al.*, “SiGe HBT with $f_T\,/\,f_{\max}$ of 505 GHz /720 GHz,” in *Proc. IEEE Int. Electron Devices Meeting*, San Francisco, CA, USA, 2016, pp. 3.1.1–3.1.4, doi: 10.1109/IEDM.2016.7838335.

[42] J. Grzyb, K. Statnikov, N. Sarmah, B. Heinemann, and U. R. Pfeiffer, “A 210–270-GHz circularly polarized FMCW radar with a single-lens-coupled SiGe HBT chip,” *IEEE Trans. THz Sci. Technol.*, vol. 6, no. 6, pp. 771–783, Nov. 2016, doi: 10.1109/TTHZ.2016.2602539.

[43] S. Malz, P. Hillger, B. Heinemann, and U. R. Pfeiffer, “A 275 GHz amplifier in 0.13 μm SiGe,” in *Proc. 11th Eur. Microw. Integr. Circuits Conf.*, London, U.K., 2016, pp. 185–188, doi: 10.1109/EuMIC.2016.7777521.

[44] M. H. Eissa *et al.*, “Wideband 240-GHz transmitter and receiver in BiCMOS technology with 25-Gbit/s data rate,” *IEEE J. Solid-State Circuits*, vol. 53, no. 9, pp. 2532–2542, Sep. 2018, doi: 10.1109/JSSC.2018.2839037.

[45] I. Post *et al.*, “A 65 nm CMOS SOC technology featuring strained silicon transistors for RF applications,” in *IEEE Int. Electron Devices Meeting*, San Francisco, CA, USA, 2006, pp. 1–3, doi: 10.1109/IEDM.2006.346816.

[46] C. A. Balanis, *Advanced Engineering Electromagnetics*. Hoboken, NJ, USA: Wiley, 2012.

[47] K. Sengupta, D. Seo, L. Yang, and A. Hajimiri, “Silicon integrated 280 GHz imaging chipset with 4 × 4 SiGe receiver array and CMOS source,” *IEEE Trans. THz Sci. Technol.*, vol. 5, no. 3, pp. 427–437, May 2015, doi: 10.1109/TTHZ.2015.2414826.

[48] D. Filipovic, S. Gearhart, and G. Rebeiz, “Double-slot antennas on extended hemispherical and elliptical silicon dielectric lenses,” *IEEE Trans. THz Sci. Technol.*, vol. 41, no. 10, pp. 1738–1749, Oct. 1993, doi: 10.1109/22.247919.

[49] E. Seok *et al.*, “A 410 GHz CMOS push-push oscillator with an on-chip patch antenna,” in *Proc. IEEE Int. Solid-State Circuits Conf.*, San Francisco, CA, USA, Feb. 2008, pp. 472–629, doi: 10.1109/ISSCC.2008.4523262.

[50] O. Momeni and E. Afshari, “High power terahertz and milimeter-wave oscillator design: A systematic approach,” *IEEE J. Solid-State Circuits*, vol. 46, no. 3, pp. 583–597, Mar. 2011, doi: 10.1109/jssc.2011.2104553.

[51] H. Aghasi, A. Cathelin, and E. Afshari, “A 0.92-THz SiGe power radiator based on a nonlinear theory for harmonic generation,” *IEEE J. Solid-State Circuits*, vol. 52, no. 2, pp. 406–422, Feb. 2017, doi: 10.1109/jssc.2016.2627547.

[52] P. Hillger, J. Grzyb, S. Malz, B. Heinemann, and U. Pfeiffer, “A lens-integrated 430 GHz SiGe HBT source with up to −6.3 dBm radiated power,” in *Proc. IEEE Radio Freq. Integr. Circuits Symp.*, Honolulu, HI, USA, Jun. 2017, pp. 160–163, doi: 10.1109/rfic.2017.7969042.

[53] U. R. Pfeiffer *et al.*, “A 0.53 THz reconfigurable source module with up to 1 mW radiated power for diffuse illumination in terahertz imaging applications,” *IEEE J. Solid-State Circuits*, vol. 49, no. 12, pp. 2938–2950, Dec. 2014, doi: 10.1109/JSSC.2014.2358570.

[54] R. Han and E. Afshari, “A CMOS high-power broadband 260-GHz radiator array for spectroscopy,” *IEEE J. Solid-State Circuits*, vol. 48, no. 12, pp. 3090–3104, Dec. 2013, doi: 10.1109/JSSC.2013.2272864.

[55] J. Grzyb, Y. Zhao, and U. R. Pfeiffer, “A 288-GHz lens-integrated balanced triple-push source in a 65-nm CMOS technology,” *IEEE J. Solid-State Circuits*, vol. 48, no. 7, pp. 1751–1761, Jul. 2013, doi: 10.1109/JSSC.2013.2253403.

[56] S. Jameson and E. Socher, “High efficiency 293 GHz radiating source in 65 nm CMOS,” *IEEE Microw. Wireless Compon. Lett.*, vol. 24, no. 7, pp. 463–465, Jul. 2014, doi: 10.1109/LMWC.2014.2316210.

[57] J. Al-Eryani, H. Knapp, J. Kammerer, K. Aufinger, H. Li, and L. Maurer, “Fully integrated single-chip 305–375-GHz transceiver with on-chip antennas in SiGe BiCMOS,” *IEEE Trans. THz Sci. Technol.*, vol. 8, no. 3, pp. 329–339, May 2018, doi: 10.1109/TTHZ.2018.2823202.

[58] L. Wu, S. Liao, and Q. Xue, “A 312-GHz CMOS injection-locked radiator with chip-and-package distributed antenna,” *IEEE J. Solid-State Circuits*, vol. 52, no. 11, pp. 2920–2933, Nov. 2017, doi: 10.1109/JSSC.2017.2727046.

[59] P. Hillger, J. Grzyb, R. Lachner, and U. Pfeiffer, “An antenna-coupled 0.49 THz SiGe HBT source for active illumination in terahertz imaging applications,” in *Proc. 10th Eur. Microw. Integr. Circuits Conf.*, Paris, France, Sep. 2015, pp. 180–183, doi: 10.1109/eumic.2015.7345098.

[60] K. Guo, A. Standaert, and P. Reynaert, “A 525–556-GHz radiating source with a dielectric lens antenna in 28-nm CMOS,” *IEEE Trans. THz Sci. Technol.*, vol. 8, no. 3, pp. 340–349, May 2018, doi: 10.1109/TTHZ.2018.2815783.

[61] B. Khamaisi, S. Jameson, and E. Socher, “0.61 THz radiating source with on-chip antenna on 65 nm CMOS,” in *Proc. 11th Eur. Microw. Integr. Circuits Conf.*, London, U.K., Oct. 2016, pp. 389–392, doi: 10.1109/EuMIC.2016.7777573.

[62] Y. Yang, O. D. Gurbuz, and G. M. Rebeiz, “An eight-element 370–410-GHz phased-array transmitter in 45-nm CMOS SOI with peak EIRP of 8–8.5 dBm,” *IEEE Trans. THz Sci. Technol.*, vol. 64, no. 12, pp. 4241–4249, Dec. 2016, doi: 10.1109/TMTT.2016.2613850.

[63] F. Golcuk, O. D. Gurbuz, and G. M. Rebeiz, “A 0.39–0.44 THz 2 × 4 amplifier-quadrupler array with peak EIRP of 3–4 dBm,” *IEEE Trans. Microw. Theory Techn.*, vol. 61, no. 12, pp. 4483–4491, Dec. 2013, doi: 10.1109/TMTT.2013.2287493.

[64] Y. Zhao *et al.*, “A 0.56 THz phase-locked frequency synthesizer in 65 nm CMOS technology,” *IEEE J. Solid-State Circuits*, vol. 51, no. 12, pp. 3005–3019, Dec. 2016, doi: 10.1109/JSSC.2016.2601614.

[65] B. Khamaisi, S. Jameson, and E. Socher, “A 0.58–0.61 THz single on-chip antenna transceiver based on active X30 LO chain on 65 nm CMOS,” in *Proc. 11th Euro. Microw. Integr. Circuits Conf.*, London, U.K., Oct. 2016, pp. 97–100, doi: 10.1109/eumic.2016.7777499.

[66] Z. Ahmad and K. O. Kenneth, “0.65–0.73 THz quintupler with an on-chip antenna in 65-nm CMOS,” in *Proc. Symp. VLSI Circuits*, Kyoto, Japan, Jun. 2015, pp. C310–C311, doi: 10.1109/VLSIC.2015.7231303.

[67] E. Öjefors, J. Grzyb, Y. Zhao, B. Heinemann, B. Tillack, and U. R. Pfeiffer, “A 820 GHz SiGe chipset for terahertz active imaging applications,” in *Proc. IEEE Int. Solid-State Circuits Conf.*, San Francisco, CA, USA, Feb. 2011, pp. 224–226, doi: 10.1109/isscc.2011.5746294.

[68] Z. Ahmad, M. Lee, and K. K. O, “20.5 1.4 THz, −13 dBm-EIRP frequency multiplier chain using symmetric- and asymmetric-CV varactors in 65 nm CMOS,” in *Proc. IEEE Int. Solid-State Circuits Conf.*, San Francisco, CA, USA, Jan. 2016, pp. 350–351, doi: 10.1109/isscc.2016.7418051.

[69] E. Johnson, “Physical limitations on frequency and power parameters of transistors,” in *Proc. IRE Int. Conv. Rec.*, New York, NY, USA, Mar. 1965, vol. 13, pp. 27–34, doi: 10.1109/IRECON.1965.1147520.

[70] U. R. Pfeiffer and E. Ojefors, “A 600-GHz CMOS focal-plane array for terahertz imaging applications,” in *Proc. 34th Euro. Solid-State Circuits Conf.*, Sep. 2008, pp. 110–113, doi: 10.1109/ESSCIRC.2008.4681804.

[71] F. F. Sizov, V. P. Reva, A. G. Golenkov, and V. V. Zabudsky, “Uncooled detectors challenges for THz/sub-THz arrays imaging,” *J. Infrared, Millim., THz Waves*, vol. 32, no. 10, pp. 1192–1206, Oct. 2011, doi: 10.1007/s10762-011-9789-2.

[72] J. L. Hesler and T. W. Crowe, “NEP and responsivity of THz zero-bias Schottky diode detectors,” in *Proc. Joint 32nd Int. Conf. Infrared Millim. Waves/15th Int. Conf. THz Electron.*, Sep. 2007, pp. 844–845, doi: 10.1109/ICIMW.2007.4516758.

[73] V. Radisic *et al.*, “Power amplification at 0.65 THz using InP HEMTs,” *IEEE Trans. Microw. Theory Techn.*, vol. 60, no. 3, pp. 724–729, Mar. 2012, doi: 10.1109/TMTT.2011.2176503.

[74] C. Middleton, G. Zummo, A. Weeks, A. Pergande, L. Mirth, and G. Boreman, “Passive millimeter-wave focal plane array,” in *Proc. Joint 29th Int. Conf. Infrared Millim. Waves 12th Int. Conf. THz Electron.*, Sep. 2004, pp. 745–746, doi: 10.1109/ICIMW.2004.1422307.

[75] G. Karolyi, D. Gergelyi, and P. Foldesy, “Sub-THz sensor array with embedded signal processing in 90 nm CMOS technology,” *IEEE Sensors J.*, vol. 14, no. 8, pp. 2432–2441, Aug. 2014, doi: 10.1109/JSEN.2013.2291316.

[76] S. Boppel *et al.*, “CMOS integrated antenna-coupled field-effect transistors for the detection of radiation from 0.2 to 4.3 THz,” vol. 60, no. 12, pp. 3834–3843, Dec. 2012, doi: 10.1109/TMTT.2012.2221732.

[77] A. Boukhayma, A. Dupret, J.-P. Rostaing, and C. Enz, “A low-noise CMOS THz imager based on Bource modulation and an in-pixel high-Q passive switched-capacitor N-path filter,” *Sensors*, vol. 16, no. 3, Mar. 2016, Art. no. 325, doi: 10.3390/s16030325.

[78] H. Sherry *et al.*, “Lens-integrated THz imaging arrays in 65 nm CMOS technologies,” in *Proc. IEEE Radio Freq. Integr. Circuits Symp.*, Baltimore, MD, USA, Jun. 2011, pp. 1–4, doi: 10.1109/rfic.2011.5940670.

[79] R. Jain, H. Rucker, and U. R. Pfeiffer, “Zero gate-bias terahertz detection with an asymmetric NMOS transistor,” in *Proc. 41st Int. Conf. Infrared, Millim., THz Waves*, Sep. 2016, pp. 1–2, doi: 10.1109/IRMMW-THz.2016.7758895.

[80] U. R. Pfeiffer, J. Grzyb, H. Sherry, A. Cathelin, and A. Kaiser, “Toward low-NEP room-temperature THz MOSFET direct detectors in CMOS technology,” in *Proc. 38th Int. Conf. Infrared, Millim., THz Waves*, Mainz, Germany, Sep. 2013, pp. 1–2, doi: 10.1109/irmmw-thz.2013.6665522.

[81] R. Al Hadi *et al.*, “A 1 k-pixel video camera for 0.7–1.1 terahertz imaging applications in 65-nm CMOS,” *IEEE J. Solid-State Circuits*, vol. 47, no. 12, pp. 2999–3012, Dec. 2012, doi: 10.1109/JSSC.2012.2217851.

[82] Z.-y. Liu, L.-y. Liu, J. Yang, and N.-j. Wu, “A CMOS fully integrated 860-GHz terahertz sensor,” *IEEE Trans. THz Sci. Technol.*, vol. 7, no. 4, pp. 455–465, Jul. 2017, doi: 10.1109/TTHZ.2017.2692040.

[83] D. Yoon, J. Kim, J. Yun, M. Kaynak, B. Tillack, and J.-S. Rieh, “ 300-GHz direct and heterodyne active imagers based on 0.13-μm SiGe HBT technology,” *IEEE Trans. THz Sci. Technol.*, vol. 7, no. 5, pp. 536–545, Sep. 2017, doi: 10.1109/TTHZ.2017.2715419.

[84] M. Uzunkol, O. D. Gurbuz, F. Golcuk, and G. M. Rebeiz, “A 0.32 THz SiGe 4×4 imaging array using high-efficiency on-chip antennas,” *IEEE J. Solid-State Circuits*, vol. 48, no. 9, pp. 2056–2066, Sep. 2013, doi: 10.1109/JSSC.2013.2262739.

[85] R. Al Hadi, J. Grzyb, B. Heinemann, and U. R. Pfeiffer, “A terahertz detector array in a SiGe HBT technology,” *IEEE J. Solid-State Circuits*, vol. 48, no. 9, pp. 2002–2010, Sep. 2013, doi: 10.1109/JSSC.2013.2265493.

[86] J. Grzyb, B. Heinemann, and U. R. Pfeiffer, “Solid-state terahertz super-resolution imaging device in 130-nm SiGe BiCMOS technology,” *IEEE Trans. Microw. Theory Techn.*, vol. 65, no. 11, pp. 4357–4372, Nov. 2017, doi: 10.1109/TMTT.2017.2684120.

[87] R. Han *et al.*, “Active terahertz imaging using Schottky diodes in CMOS: Array and 860-GHz pixel,” *IEEE J. Solid-State Circuits*, vol. 48, no. 10, pp. 2296–2308, Oct. 2013, doi: 10.1109/JSSC.2013.2269856.

[88] S. V. Thyagarajan, S. Kang, and A. M. Niknejad, “A 240 GHz fully integrated wideband QPSK receiver in 65 nm CMOS,” *IEEE J. Solid-State Circuits*, vol. 50, no. 10, pp. 2268–2280, Oct. 2015, doi: 10.1109/JSSC.2015.2467216.

[89] P. R. Vazquez, J. Grzyb, N. Sarmah, B. Heinemann, and U. Pfeiffer, “A 219–266 GHz LO-tunable direct-conversion IQ receiver module in a SiGe HBT technology,” *Int. J. Microw. Wireless Technol.*, vol. 10, no. 5–6, pp. 587–595, May 2018, doi: 10.1017/S1759078718000302.

[90] J. Park, S. Kang, S. V. Thyagarajan, E. Alon, and A. M. Niknejad, “A 260 GHz fully integrated CMOS transceiver for wireless chip-to-chip communication,” in *Proc. Symp. VLSI Circuits*, Honolulu, HI, USA, Jun. 2012, pp. 48–49, doi: 10.1109/vlsic.2012.6243783.

[91] C.-H. Li, C.-L. Ko, M.-C. Kuo, and D.-C. Chang, “A 340-GHz heterodyne receiver front end in 40-nm CMOS for THz biomedical imaging applications,” *IEEE Trans. THz Sci. Technol.*, vol. 6, no. 4, pp. 625–636, Jul. 2016, doi: 10.1109/TTHZ.2016.2566580.

[92] E. Öjefors and U. R. Pfeiffer, “A 650 GHz SiGe receiver front-end for terahertz imaging arrays,” in *Proc. IEEE Int. Solid-State Circuits Conf.*, San Francisco, CA, USA, Feb. 2010, pp. 430–431, doi: 10.1109/isscc.2010.5433886.

[93] Z. Ahmad and K. K O, “THz detection using p+/n-well diodes fabricated in 45-nm CMOS,” *IEEE Electron Device Lett.*, vol. 37, no. 7, pp. 823–826, Jul. 2016, doi: 10.1109/led.2016.2573268.

[94] D. Y. Kim, S. Park, R. Han, and K. K O, “Design and demonstration of 820-GHz array using diode-connected NMOS transistors in 130-nm CMOS for active imaging,” *IEEE Trans. THz Sci. Technol.*, vol. 6, no. 2, pp. 306–317, Mar. 2016, doi: 10.1109/TTHZ.2015.2513061.

[95] B. B. Hu and M. C. Nuss, “Imaging with terahertz waves,” *Opt. Lett.*, vol. 20, no. 16, pp. 1716–1718, Aug. 1995, doi: 10.1364/ol.20.001716.

[96] L. Öhrström, A. Bitzer, M. Walther, and F. J. Rühli, “Technical note: Terahertz imaging of ancient mummies and bone,” *Amer. J. Phys. Anthropol.*, vol. 142, no. 3, pp. 497–500, Apr. 2010, doi: 10.1002/ajpa.21292.

[97] J.-P. Caumes *et al.*, “Terahertz tomographic imaging of XVIIIth dynasty Egyptian sealed pottery,” *Appl. Opt.*, vol. 50, no. 20, pp. 3604–3608, Jul. 2011, doi: 10.1364/AO.50.003604.

[98] M. Bessou *et al.*, “Three-dimensional terahertz computed tomography of human bones,” *Appl. Opt.*, vol. 51, no. 28, pp. 6738–6744, Oct. 2012, doi: 10.1364/ao.51.006738.

[99] J. Takayanagi *et al.*, “High-resolution time-of-flight terahertz tomography using a femtosecond fiber laser,” *Opt. Express*, vol. 17, no. 9, pp. 7533–7539, Apr. 2009, doi: 10.1364/oe.17.007533.

[100] B. Ferguson, S. Wang, D. Gray, D. Abbot, and X.-C. Zhang, “T-ray computed tomography,” *Opt. Lett.*, vol. 27, no. 15, pp. 1312–1314, Aug. 2002, doi: 10.1364/ol.27.001312.

[101] S. Wang and X.-C. Zhang, “Tomographic imaging with a terahertz binary lens,” *Appl. Phys. Lett.*, vol. 82, no. 12, pp. 1821–1823, Mar. 2003, doi: 10.1063/1.1563043.

[102] A. Brahm, M. Kunz, S. Riehemann, G. Notni, and A. Tünnermann, “Volumetric spectral analysis of materials using terahertz-tomography techniques,” *Appl. Phys. B*, vol. 100, no. 1, pp. 151–158, Jul. 2010, doi: 10.1007/s00340-010-3945-6.

[103] M. González-Cardel, P. Arguijo, and R. Díaz-Uribe, “Gaussian beam radius measurement with a knife-edge: A polynomial approximation to the inverse error function,” *Appl. Opt.*, vol. 52, no. 16, pp. 3849–3855, Jun. 2013, doi: 10.1364/AO.52.003849.

[104] W. van Aarle *et al.*, “The ASTRA toolbox: A platform for advanced algorithm development in electron tomography,” *Ultramicroscopy*, vol. 157, pp. 35–47, Oct. 2015, doi: 10.1016/J.ULTRAMIC.2015.05.002.

[105] M. Jewariya *et al.*, “Fast three-dimensional terahertz computed tomography using real-time line projection of intense terahertz pulse,” *Opt. Express*, vol. 21, no. 2, pp. 2423–2433, Jan. 2013, doi: 10.1364/OE.21.002423.

[106] G. C. Trichopoulos and K. Sertel, “Broadband terahertz computed tomography using a 5 k-pixel real-time THz camera,” *J. Infrared, Millim., THz Waves*, vol. 36, pp. 675–686, Feb. 2015, doi: 10.1007/s10762-015-0144-x.

[107] M. F. Duarte *et al.*, “Single-pixel imaging via compressive sampling,” *IEEE Signal Process. Mag.*, vol. 25, no. 2, pp. 83–91, Mar. 2008, doi: 10.1109/msp.2007.914730.

[108] W. L. Chan, K. Charan, D. Takhar, K. F. Kelly, R. G. Baraniuk, and D. M. Mittleman, “A single-pixel terahertz imaging system based on compressed sensing,” *Appl. Phys. Lett.*, vol. 93, no. 12, Mar. 2008, Art. no. 121105, doi: 10.1063/1.2989126.

[109] S. Augustin, J. Hieronymus, P. Jung, and H.-W. Hübers, “Compressed sensing in a fully non-mechanical 350 GHz imaging setting,” *J. Infrared, Millim., Terahertz Waves*, vol. 36, no. 5, pp. 496–512, May 2015, doi: 10.1007/s10762-014-0141-5.

[110] R. I. Stantchev *et al.*, “Noninvasive, near-field terahertz imaging of hidden objects using a single-pixel detector,” *Sci. Adv.*, vol. 2, no. 6, Jun. 2016, Art. no. e1600190, doi: 10.1126/sciadv.1600190.

[111] C. M. Watts *et al.*, “Terahertz compressive imaging with metamaterial spatial light modulators,” *Nature Photon.*, vol. 8, no. 8, p. 605, Jun. 2014, DOI 10.1038/nphoton.2014.139.

[112] M. H. Conde, K. Hartmann, and O. Loffeld, “Simple adaptive progressive edge-growth construction of LDPC codes for close(r)-to-optimal sensing in pulsed TOF,” in *Proc. 4th Int. Workshop Compressed Sens. Theory Its Appl. Radar, Sonar Remote Sens.*, Aachen, Germany, Sep. 2016, pp. 80–84, doi: 10.1109/cosera.2016.7745704.

[113] K. Kawase, Y. Ogawa, Y. Watanabe, and H. Inoue, “Non-destructive terahertz imaging of illicit drugs using spectral fingerprints,” *Opt. Express*, vol. 11, no. 20, pp. 2549–2554, Oct. 2003, doi: 10.1364/OE.11.002549.

[114] Y. C. Shen, T. Lo, P. F. Taday, B. E. Cole, W. R. Tribe, and M. C. Kemp, "Detection and identification of explosives using terahertz pulsed spectroscopic imaging," *Appl. Phys. Lett.*, vol. 86, no. 24, Jun. 2005, Art. no. 241116, doi: 10.1063/1.1946192.

[115] K. Schmalz, N. Rothbart, P. F.-X. Neumaier, J. Borngrber, H. Hbers, and D. Kissinger, "Gas spectroscopy system for breath analysis at mm-wave/THz using SiGe BiCMOS circuits," *IEEE Trans. THz Sci. Technol.*, vol. 65, no. 5, pp. 1807–1818, May 2017, doi: 10.1109/TMTT.2017.2650915.

[116] K. Schmalz *et al.*, "245-GHz transmitter array in SiGe BiCMOS for gas spectroscopy," *IEEE Trans. THz Sci. Technol.*, vol. 6, no. 2, pp. 318–327, Mar. 2016, doi: 10.1109/TTHZ.2015.2513278.

[117] J. Grzyb, K. Statnikov, and U. Pfeiffer, "A lens-coupled all-silicon integrated 2 × 2 array of harmonic receivers for THz multi-color active imaging," in *Proc. 9th Euro. Conf. Antennas Propag.*, Lisbon, Portugal, Apr. 2015, pp. 1–5.

[118] J. Grzyb, K. Statnikov, and U. R. Pfeiffer, "A 2 × 2 lens-integrated on-chip antenna system for a 820 GHz multiplier-chain source in SiGe technology," in *Proc. IEEE Antennas Propag. Soc. Int. Symp.*, Memphis, TN, USA, Jul. 2014, pp. 737–738, doi: 10.1109/APS.2014.6904698.

[119] K. Cooper *et al.*, "Penetrating 3-D imaging at 4- and 25-m range using a submillimeter-wave radar," *IEEE Trans. Microw. Theory Techn.*, vol. 56, no. 12, pp. 2771–2778, Dec. 2008, doi: 10.1109/TMTT.2008.2007081.

[120] J. Grajal *et al.*, "3-D high-resolution imaging radar at 300 GHz with enhanced FoV," *IEEE Trans. Microw. Theory Techn.*, vol. 63, no. 3, pp. 1097–1107, Mar. 2015, doi: 10.1109/TMTT.2015.2391105.

[121] H. Essen *et al.*, "A high performance 220-GHz broadband experimental radar," in *Proc. 33rd Int. Conf. Infrared, Millim., Terahertz Waves*, Pasadena, CA, USA, Sep. 2008, p. 1, doi: 10.1109/ICIMW.2008.4665687.

[122] C. Li, V. M. Lubecke, O. Boric-Lubecke, and J. Lin, "A review on recent advances in Doppler radar sensors for noncontact healthcare monitoring," *IEEE Trans. Microw. Theory Techn.*, vol. 61, no. 5, pp. 2046–2060, May 2013, doi: 10.1109/TMTT.2013.2256924.

[123] N. Karpowicz, H. Zhong, J. Xu, K.-I. Lin, J.-S. Hwang, and X.-C. Zhang, "Non-destructive sub-THz CW imaging," *Proc. SPIE*, vol. 5727, Mar. 2005, Art. no. 5727, doi: 10.1117/12.590539.

[124] J. Grzyb, K. Statnikov, N. Sarmah, and U. R. Pfeiffer, "A wideband 240 GHz lens-integrated circularly polarized on-chip annular slot antenna for a FMCW radar transceiver module in SiGe technology," in *Proc. SBMO/IEEE MTT-S Int. Microw. Optoelectron. Conf.*, Porto de Galinhas, Brazil, Nov. 2015, pp. 1–4, doi: 10.1109/imoc.2015.7369165.

[125] J. Grzyb, K. Statnikov, N. Sarmah, and U. R. Pfeiffer, "A broadband 240 GHz lens-integrated polarization-diversity on-chip circular slot antenna for a power source module in SiGe technology," in *Proc. Euro. Microw. Conf.*, Paris, France, Sep. 2015, pp. 570–573, doi: 10.1109/eumc.2015.7345827.

[126] M. Jahn and A. Stelzer, "A 120 GHz FMCW radar frontend demonstrator based on a SiGe chipset," *Int. J. Microw. Wireless Technol.*, vol. 4, no. 03, pp. 309–315, Jun. 2012, doi: 10.1017/S1759078712000323.

[127] T. Jaeschke, C. Bredendiek, and N. Pohl, "A 240 GHz ultra-wideband FMCW radar system with on-chip antennas for high resolution radar imaging," in *Proc. IEEE MTT-S Int. Microw. Symp. Dig.*, Seattle, WA, USA, Jun. 2013, pp. 1–4, doi: 10.1109/MWSYM.2013.6697495.

[128] M. Moallem and K. Sarabandi, "Polarimetric study of MMW imaging radars for indoor navigation and mapping," *IEEE Antennas Propag. Mag.*, vol. 62, no. 1, pp. 500–504, Jan. 2014, doi: 10.1109/TAP.2013.2289354.

[129] N. Sarmah *et al.*, "A fully integrated 240-GHz direct-conversion quadrature transmitter and receiver chipset in SiGe technology," *IEEE Trans. Microw. Theory Techn.*, vol. 64, no. 2, pp. 562–574, Feb. 2016, doi: 10.1109/TMTT.2015.2504930.

[130] F. J. Harris, "On the use of windows for harmonic analysis with the discrete Fourier transform," *Proc. IEEE*, vol. 66, no. 1, pp. 51–83, Jan. 1978, doi: 10.1109/PROC.1978.10837.

[131] A. J. Huber, F. Keilmann, J. Wittborn, J. Aizpurua, and R. Hillenbrand, "Terahertz near-field nanoscopy of mobile carriers in single semiconductor nanodevices," *Nano Lett.*, vol. 8, no. 11, pp. 3766–3770, Nov. 2008, doi: 10.1021/nl802086x.

[132] O. Mitrofanov *et al.*, "Terahertz near-field microscopy based on a collection mode detector," *Appl. Phys. Lett.*, vol. 77, no. 22, pp. 3496–3498, Nov. 2000, doi: 10.1063/1.1328772.

[133] O. Mitrofanov *et al.*, "Collection-mode near-field imaging with 0.5-THz pulses," *IEEE J. Sel. Topics Quantum Electron.*, vol. 7, no. 4, pp. 600–607, Jul. 2001, doi: 10.1109/2944.974231.

[134] H.-T. Chen, R. Kersting, and G. C. Cho, "Terahertz imaging with nanometer resolution," *Appl. Phys. Lett.*, vol. 83, no. 15, pp. 3009–3011, Oct. 2003, doi: 10.1063/1.1616668.

[135] A. J. L. Adam, "Review of near-field terahertz measurement methods and their applications," *J. Infrared, Millim., Terahertz Waves*, vol. 32, no. 8, Jul. 2011, Art. no. 976, doi: 10.1007/s10762-011-9809-2.

[136] Y. Kawano and K. Ishibashi, "An on-chip near-field terahertz probe and detector," *Nature Photon.*, vol. 2, no. 10, pp. 618–621, Aug. 2008, doi: 10.1038/nphoton.2008.157.

[137] J. Szelc and H. Rutt, "Near-Field THz imaging and spectroscopy using a multiple subwavelength aperture modulator," *IEEE Trans. THz Sci. Technol.*, vol. 3, no. 2, pp. 165–171, Mar. 2013, doi: 10.1109/TTHZ.2012.2232812.

[138] P. Hillger *et al.*, "A solid-state 0.56 THz near-field array for μ M-scale surface imaging," in *Proc. 43rd Int. Conf. Infrared, Millim., Terahertz Waves*, Nagoya, Japan, Sep. 2018, pp. 1–2, doi: 10.1109/IRMMW-THz.2018.8509876.

Philipp Hillger (GS'15–M'17) received the B.Sc. and M.Sc. degrees in electrical engineering from the Ruhr-University Bochum, Bochum, Germany, in 2011 and 2014, respectively, and is currently working toward the Ph.D. degree at the Institute for High-Frequency and Communication Technology, Wuppertal, Germany.

From 2011 to 2013, he was with Intel Mobile Communications, Duisburg, Germany, where he was involved in IC design and system engineering for various wireless standards. His major fields of interest are silicon-based mmWave and THz systems for imaging, sensing, and communication.

Janusz Grzyb received the M.Sc. (*cum laude*) degree in electronic engineering from the Integrated Circuits Laboratory, Technical University of Gdańsk, Gdańsk, Poland, in 1998, where he majored in the synthesis and design of analog CMOS and BiCMOS circuits with an individual study program, and the Ph.D. degree from the Swiss Federal Institute of Technology, Zurich, Switzerland, in 2004.

He was a Research Assistant with the Technical University of Gdańsk, from 1998 to 1999. In 1999, he joined the Electronics Labs, Swiss Federal Institute of Technology, Zurich, Switzerland, where he performed pioneering work in the area of low-cost large area panel processing MCM-based SiP solutions for 60, 77, and 94 GHz applications. From 2004 to 2006, he was with the Communication System Design and High-Speed/Optical Packaging Groups, IBM T. J. Watson Research Center, Yorktown Heights, NY, USA, where he was involved in the development of the low-cost packaged highly integrated SiGe transceiver for 60-GHz Gb/s wireless data communication. From 2006 to 2009, he was with the Research and Development Group, Huber&Suhner, Pfäffikon, Switzerland, where he brought into the market one of the world's first commercially available point-to-point 60-GHz links: the Sensity Link System. Since 2009, he has been with the Institute for High-Frequency and Communication Technology, University of Wuppertal, Wuppertal, Germany. His current research interests include all aspects of silicon-integrated terahertz electronics.

Dr. Grzyb was a co-recipient of the 2006 Lewis Winner Award for Outstanding Paper of the IEEE International Solid-State Circuit Conference, the 2006 IBM Pat Goldberg Memorial Best Paper Award, the 2012 Jan Van Vessem Award for Outstanding European Paper of the IEEE International Solid State Circuits Conference, the 2014 Best Paper Award of the European Conference on Antennas and Propagation, and the Microwave Prize 2017 of the IEEE Microwave Theory and Techniques Society.

Ritesh Jain received the Master of Technology degree in electrical engineering from the Indian Institute of Technology Gandhinagar, Ahmedabad, India, in 2014.

During 2013–2014, he was a joint Research Fellow with the Technical University of Berlin, Berlin, Germany, and the IHP Microelectronics, Frankfurt (Oder), Germany, under the DAAD-IIT Master Sandwich Program. He is currently a Research Assistant with the Institute for High-Frequency and Communication Technology, University of Wuppertal, Wuppertal, Germany. His current research interests include all aspects of silicon-integrated terahertz electronics.

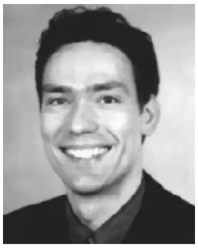

Ullrich R. Pfeiffer (M'02–SM'06) received the Diploma degree in physics and the Ph.D. degree in physics from the University of Heidelberg, Heidelberg, Germany, in 1996 and 1999, respectively.

In 1997, he was a Research Fellow with the Rutherford Appleton Laboratory, Harwell, U.K. From 1999 to 2001, he was a Postdoctoral Researcher with the University of Heidelberg on real-time electronics for particle physics experiments at the European Organization for Nuclear Research (CERN), Switzerland. From 2001 to 2006, he was with the IBM T. J. Watson Research Center, where his research involved RF circuit design, power amplifier design at 60 and 77 GHz, high-frequency modeling, and packaging for millimeter-wave communication systems. In 2007, he led the THz Electronics Group, Institute of High-Frequency and Quantum Electronics at the University of Siegen, Germany. Since 2008, he has been the High-frequency and Communication Technology Chair with the University of Wuppertal, Germany. His current research includes silicon RFICs for mmWave/THz communication, radar, and imaging systems.

Dr. Pfeiffer was the recipient of a European Young Investigator Award in 2007. He was the co-recipient of the 2004 and 2006 Lewis Winner Award for Outstanding Paper of the IEEE International Solid-State Circuit Conference, the co-recipient of the 2006 IBM Pat Goldberg Memorial Best Paper Award, the 2008 EuMIC Best Paper Award, the 2010 EuMC Microwave Prize, the 2012 Jan Van Vessem Award for Outstanding European Paper of the 2012 IEEE International Solid-State Circuit Conference, the 2014 EuCAP Best Paper Award, and the 2017 Microwave Prize. He has been a Distinguished Lecturer of the IEEE Solid-State Circuits Society and the President of the German Association for Electrical Engineering and Information Technology e.V. (FTEI).